J. Fluid Mech. (1999), *vol.* 400, *pp.* 125–162. Printed in the United Kingdom

Non-similarity solutions to the corner boundary-layer equations (and the effects of wall transpiration)

By PETER W. DUCK[1], SIMON R. STOW[1] AND MANHAR R. DHANAK[2]

[1]Department of Mathematics, University of Manchester, Manchester M13 9PL, UK

[2]Department of Ocean Engineering, Florida Atlantic University, Boca Raton, Florida, 33431, USA

(Received 8 December 1997 and in revised form 5 July 1999)

The incompressible boundary layer in the corner formed by two intersecting, semi-infinite planes is investigated, when the free-stream flow, aligned with the corner, is taken to be of the form $U_\infty F(x)$, x representing the non-dimensional streamwise distance from the leading edge. In Dhanak & Duck (1997) similarity solutions for $F(x) = x^n$ were considered, and it was found that solutions exist for only a range of values of n, whilst for $\infty > n > -0.018$, approximately, two solutions exist. In this paper, we extend the work of Dhanak & Duck to the case of non-90° corner angles and allow for streamwise development of solutions. In addition, the effect of transpiration at the walls of the corner is investigated. The governing equations are of boundary-layer type and as such are parabolic in nature. Crucially, although the leading-order pressure term is known *a priori*, the third-order pressure term is not, but this is nonetheless present in the leading-order governing equations, together with the transverse and crossflow viscous terms.

Particular attention is paid to flows which develop spatially from similarity solutions. It turns out that two scenarios are possible. In some cases the problem may be treated in the usual parabolic sense, with standard numerical marching procedures being entirely appropriate. In other cases standard marching procedures lead to numerically inconsistent solutions. The source of this difficulty is linked to the existence of eigensolutions emanating from the leading edge (which are not present in flows appropriate to the first scenario), analogous to those found in the computation of some two-dimensional hypersonic boundary layers (Neiland 1970; Mikhailov *et al.* 1971; Brown & Stewartson 1975). In order to circumvent this difficulty, a different numerical solution strategy is adopted, based on a global Newton iteration procedure.

A number of numerical solutions for the entire corner flow region are presented.

1. Introduction

The viscous flow along a corner formed by two intersecting flat plates has received a good deal of attention over the years, due to the importance of flows associated with wing–body junctions in numerous aerospace (and other) applications. The first fully rigorous treatment of such flows at high Reynolds numbers was made by Rubin (1966), who presented the structure of the solution for problems of this type.

Perhaps the crucial feature of the problem highlighted in that paper is that the third-order pressure term, generally neglected in classical, two-dimensional boundary-layer theory, plays a pivotal role in corner regions, and is coupled at leading order with other, convective and viscous quantities. Similarity solutions for situations involving constant free-stream velocities (in which the streamwise development of the flow may be scaled into the solution), have been calculated by a number of authors (including Rubin 1966; Pal & Rubin 1971; Rubin & Grossman 1971; Desai & Mangler 1974; Ghia 1975; Zamir 1973).

The condition of constant free-stream velocity was relaxed by Dhanak & Duck (1997, hereafter referred to as DD) to consider spatially varying flows with free-stream velocity of the form x^n, x denoting the non-dimensional distance from the leading edge, as in the classical Falkner–Skan problem in two-dimensional boundary-layer theory. In DD, we showed that (i) solutions are not possible for all values of n, and (ii) a primary solution branch exists in parameter space for $\infty > n > -0.018$, approximately, for which two solutions exist. These results are consistent with those of Ridha (1992), although that work is incomplete, in that (i) only a single solution branch was identified, and (ii) it was claimed that solutions only existed over a limited, finite range of n; further, only limiting solutions (valid for large distances from the corner) were considered. We retain the terminology used in DD, by referring to the upper and lower solution branches in modified wall vorticity–n space (see figure 1*a* of the present paper and figure 2*c* of DD). We show that in the zero pressure gradient case (i.e. with $n = 0$) in addition to the solution corresponding to Blasius-type far-field conditions (the conditions imposed in most previous studies), a second solution exists, comprising an accelerating, jet-like crossflow, directed away from the corner.

The question of breakdown of symmetry about the corner-bisector line was also addressed by DD. This feature was found to further complicate the flow, significantly modifying the range of the parameter n for which similarity solutions exist, and also causing further complication (including giving rise to additional solutions) to the solution branches. A heuristic approach to the stability of the flow in the corner region was also undertaken, using the ideas of Lakin & Hussaini (1984) and Dhanak (1993); this suggested that a favourable pressure gradient has a stabilizing effect while an adverse pressure gradient is destabilizing, the critical Reynolds number for the local flow becoming larger with increasing distance from the corner in all cases. An inviscid stability analysis has been undertaken by Balachandar & Malik (1995).

Taken together, these features could well go some way in explaining the difficulties noted by Zamir (1981) in observing similarity-type solutions in experiments. Certainly the results of DD suggest that any slight misalignment of the corner in an experiment could substantially disrupt the overall flow pattern in these regions. Additionally, Zamir (1981) highlights the wide spread in the available numerical results.

The purpose of the current paper is to consider more general forms of the streamwise velocity variation, taking the solutions of the type discussed in DD as upstream conditions at the leading edge. Further, we generalize consideration to arbitrary, non-90°, corner angles using the ideas of Wilkinson & Zamir (1984). We also investigate the effects of transpiration through the walls in the presence of non-zero pressure gradient.

The layout of the paper is as follows. In § 2, we formulate the problem, initially following the approach of Rubin (1966), but then relaxing the similarity constraint by allowing general streamwise variations of the solution, although our methodology

is to use the similarity solutions of DD as upstream conditions to the problem. In §§ 3 and 4, we consider the nature of solutions at large distances from the corner, focusing our attention on the effects of wall transpiration, including both wall suction and blowing in § 3 and the similarity constraint is relaxed in § 4; these solutions are used as far-field boundary conditions in the full numerical problem, considered in § 5. In § 6 we present our conclusions.

2. Formulation

Consider two semi-infinite planes, intersecting, in Cartesian coordinates (Lx, Ly, Lz), along Ox with the origin located at the leading edge; L is a reference lengthscale (generally taken to be that arising from the scale of the freestream velocity variation). One plane is given by $y = 0$, the other by $z = y\cot\alpha$. The steady velocity is written $U_\infty(u, v, w)$, where far from both planes the x-component of velocity is $U_\infty F(x)$.

We initially follow the approach of Rubin (1966), guided by the development of classical two-dimensional boundary-layer theory, by writing

$$\left.\begin{aligned} u &= \hat{U}(x, Y, Z) + \cdots, \\ v &= Re^{-1/2}\hat{V}(x, Y, Z) + \cdots, \\ w &= Re^{-1/2}\hat{W}(x, Y, Z) + \cdots, \\ p &= P_0(x) + Re^{-1/2}P_1(x) + Re^{-1}\hat{P}(x, Y, Z) + \cdots, \end{aligned}\right\} \tag{2.1}$$

where $\rho U_\infty^2 p$ denotes the pressure (ρ being the fluid density, assumed constant), the Reynolds number $Re = U_\infty L/\nu$ and

$$Y = Re^{1/2}y, \quad Z = Re^{1/2}z, \tag{2.2}$$

are the scaled boundary-layer variables; P_0 and P_1 can easily be shown to be independent of Y and Z.

Substituting (2.1) into the Navier–Stokes and continuity equations, and retaining the leading-order terms in Re yields

$$\hat{U}\hat{U}_x + \hat{V}\hat{U}_Y + \hat{W}\hat{U}_Z = \hat{U}_{YY} + \hat{U}_{ZZ} - P_{0_x}, \tag{2.3}$$

$$\hat{U}\hat{V}_x + \hat{V}\hat{V}_Y + \hat{W}\hat{V}_Z = \hat{V}_{YY} + \hat{V}_{ZZ} - \hat{P}_Y, \tag{2.4}$$

$$\hat{U}\hat{W}_x + \hat{V}\hat{W}_Y + \hat{W}\hat{W}_Z = \hat{W}_{YY} + \hat{W}_{ZZ} - \hat{P}_Z, \tag{2.5}$$

$$\hat{U}_x + \hat{V}_Y + \hat{W}_Z = 0. \tag{2.6}$$

The boundary conditions are that $\hat{U} = \hat{W} = 0$, $\hat{V} = V_w(x, Z)$ on the wall $Y = 0$ and $\hat{U} = \hat{V}\sin\alpha + \hat{W}\cos\alpha = 0$, $\hat{W}\sin\alpha - \hat{V}\cos\alpha = V_w(x, Y\,\mathrm{cosec}\,\alpha)$ on $Z = Y\cot\alpha$. As the free stream is approached, $\hat{U} \to F(x)$, and we have from (2.3) that to leading order the pressure gradient is given by

$$P_{0_x} = -F_x F. \tag{2.7}$$

The $O(Re^{-1})$ correction to the pressure is crucial in the following analysis, but is unknown *a priori*. Other conditions, in particular those at large distances from the corner, but close to either wall, will be discussed later.

In DD, the analysis was restricted to $F(x)$ of the form x^n (and in most other previous studies to $F(x) =$ constant); here we relax this constraint, and instead write

$$F(x) = x^n f^*(x), \tag{2.8}$$

with $f^*(0) = 1$. This implies that in the limit $x \to 0$ we obtain the similarity solutions of DD which provide upstream/initial conditions for streamwise-developing solutions.

The next step in the analysis is to introduce similarity variables in the streamwise and crossflow directions. It should be noted that this does not preclude the study of non-similarity solutions, provided $f^*(x)$ is non-constant, but rather leads to a more natural treatment of conditions as $x \to 0$.

We write

$$\hat{U} = x^n U^*(\xi, \eta^*, \zeta^*), \tag{2.9}$$

$$\hat{V} = x^{(n-1)/2} V^*(\xi, \eta^*, \zeta^*) = \frac{x^{(n-1)/2}}{\sqrt{2}} \left[(1-n)\eta^* U^* - \Phi^*\right], \tag{2.10}$$

$$\hat{W} = x^{(n-1)/2} W^*(\xi, \eta^*, \zeta^*) = \frac{x^{(n-1)/2}}{\sqrt{2}} \left[(1-n)\zeta^* U^* - \Psi^*\right], \tag{2.11}$$

$$P_0 = -\tfrac{1}{2} x^{2n} f^2(\xi), \tag{2.12}$$

$$\hat{P} = x^{n-1} P(\xi, \eta^*, \zeta^*), \tag{2.13}$$

where

$$\xi = x^{(1-n)/2}, \quad \eta^* = Y/\sqrt{2}\xi, \quad \zeta^* = Z/\sqrt{2}\xi, \quad f^*(x) = f(\xi). \tag{2.14}$$

We introduce a further variable, θ, which denotes a modified vorticity function, namely

$$\theta^* = \Psi^*_{\eta^*} - \Phi^*_{\zeta^*}. \tag{2.15}$$

Note that we may write

$$\Phi^* = (1-n)\eta^* U^* - \sqrt{2} V^*, \quad \Psi^* = (1-n)\zeta^* U^* - \sqrt{2} W^*. \tag{2.16}$$

We now introduce the variables suggested by Wilkinson & Zamir (1984) (also utilized for similarity solutions for flows with pressure gradient by Abdulwanis 1997), for arbitrary corner angle α,

$$\Phi^*(\xi, \eta^*, \zeta^*) = \Phi(\xi, \eta, \zeta), \tag{2.17}$$

$$\Psi^*(\xi, \eta^*, \zeta^*) = \Phi \cot\alpha + \Psi \operatorname{cosec}\alpha, \tag{2.18}$$

$$\theta^*(\xi, \eta^*, \zeta^*) = \theta(\xi, \eta, \zeta), \tag{2.19}$$

$$U^*(\xi, \eta^*, \zeta^*) = U(\xi, \eta, \zeta), \tag{2.20}$$

$$\eta^* = \eta \sin\alpha, \tag{2.21}$$

$$\zeta^* = \eta \cos\alpha + \zeta. \tag{2.22}$$

Implementing these transformations in (2.3)–(2.6) and eliminating the (third-order) pressure term yields the following set of equations:

$$2U \sin\alpha + (1-n)\xi \sin\alpha U_\xi = \Phi_\eta + \Psi_\zeta, \tag{2.23}$$

$$U_{\eta\eta} + U_{\zeta\zeta} + 2nf^2 \sin^2\alpha + (1-n)\sin^2\alpha \xi f f_\xi = 2nU^2 \sin^2\alpha + (1-n)\xi \sin^2\alpha U U_\xi - \Phi U_\eta \sin\alpha - \Psi U_\zeta \sin\alpha + 2\cos\alpha U_{\zeta\eta}, \tag{2.24}$$

$$\theta \sin^2\alpha = \Psi_\eta - \Phi_\zeta + \cos\alpha(\Phi_\eta - \Psi_\zeta), \tag{2.25}$$

$$\theta_{\eta\eta} + \theta_{\zeta\zeta} - 2\theta_{\eta\zeta}\cos\alpha + 2(1-n^2)\sin\alpha[(\zeta\cos\alpha+\eta)UU_\zeta - (\eta\cos\alpha+\zeta)UU_\eta]$$
$$+ \Phi\theta_\eta\sin\alpha + \Psi\theta_\zeta\sin\alpha + 2U\theta\sin^2\alpha + (n-1)\xi\{-\theta U_\xi\sin^2\alpha - U_\zeta\Phi_\xi$$
$$+ U\theta_\xi\sin^2\alpha + \Phi_\xi U_\eta\cos\alpha + \Psi_\xi U_\eta - \Psi_\xi U_\zeta\cos\alpha\} = 0. \tag{2.26}$$

The boundary conditions are then

$$\left.\begin{array}{l} U(\xi,\eta=0,\zeta) = U(\xi,\eta,\zeta=0) = 0, \\ \Phi(\xi,\eta=0,\zeta) = \Phi_w(\xi,\zeta), \quad \Psi(\xi,\eta=0,\zeta) = -\Phi_w(\xi,\zeta)\cos\alpha, \\ \Psi(\xi,\eta,\zeta=0) = \Phi_w(\xi,\eta), \quad \Phi(\xi,\eta,\zeta=0) = -\Phi_w(\xi,\eta)\cos\alpha, \end{array}\right\} \tag{2.27}$$

together with

$$\theta(\xi,\eta\to\infty,\zeta\to\infty)\to 0, \tag{2.28}$$

and

$$U(\xi,\eta\to\infty,\zeta\to\infty)\to f(\xi), \tag{2.29}$$

with $\eta/\zeta = O(1)$. In the above we have written

$$V_w = -\frac{x^{n-1}}{\sqrt{2}}\Phi_w(\xi,\zeta). \tag{2.30}$$

We shall generally assume throughout that $\Phi_w(\xi,\zeta) = O(1)$ as $\zeta\to\infty$.

The advantage of the choice of variables, in particular (2.17)–(2.22), is now clear, namely that in the case of symmetrical flows, symmetry is retained with respect to the (η,ζ) coordinate system. Thus

$$\theta(\xi,\eta,\zeta) = -\theta(\xi,\zeta,\eta), \quad U(\xi,\eta,\zeta) = U(\xi,\zeta,\eta), \quad \Phi(\xi,\eta,\zeta) = \Psi(\xi,\zeta,\eta). \tag{2.31}$$

Note that on setting $\alpha = 90^\circ$ and $\xi = 0$ in the system (2.23)–(2.26) we recover the system (2.9)–(2.12) in DD, and consequently the latter provide the upstream conditions at $\xi = 0$. In DD, asymmetrical cases were also considered, however here we confine our attention to symmetrical flows in order not to over-complicate the choice of parameter space under consideration. Henceforth, we therefore focus attention on flow in the region $\eta \leqslant \zeta$; the flow in the region $\eta > \zeta$ can be deduced from symmetry considerations. Further, in DD it was very clear that the nature of the $\zeta\to\infty$ (or $\eta\to\infty$) solutions is absolutely crucial (*a*) to understand the nature of solutions in the parameter space and (*b*) for the accurate imposition of far-field boundary conditions. It turns out that this is equally true here.

Suppose that we consider the limit $\zeta\to\infty$, $\eta\leqslant\zeta$. In this limit we expect

$$U(\xi,\eta,\zeta) = U_0(\xi,\eta) + \frac{1}{\zeta}U_1(\xi,\eta) + O(\zeta^{-2}), \tag{2.32}$$

$$\Phi(\xi,\eta,\zeta) = \Phi_0(\xi,\eta) + \frac{1}{\zeta}\Phi_1(\xi,\eta) + O(\zeta^{-2}), \tag{2.33}$$

$$\Psi(\xi,\eta,\zeta) = \zeta\Psi_0(\xi,\eta) + \Psi_1(\xi,\eta) + O(\zeta^{-1}), \tag{2.34}$$

$$\theta(\xi,\eta,\zeta) = \zeta\theta_0(\xi,\eta) + \theta_1(\xi,\eta) + O(\zeta^{-1}). \tag{2.35}$$

The leading-order terms in the expansions, when substituted into the system (2.23)–(2.26) yield

$$2U_0\sin\alpha + (1-n)\xi\sin\alpha U_{0\xi} = \Phi_{0\eta} + \Psi_0, \tag{2.36}$$

$$U_{0\eta\eta} + 2n\sin^2\alpha f^2 + \xi(1-n)\sin^2\alpha f f_\xi = 2n\sin^2\alpha U_0^2 + \xi(1-n)\sin^2\alpha U_0 U_{0\xi} - \sin\alpha \Phi_0 U_{0\eta}, \quad (2.37)$$

$$\sin^2\alpha\theta_0 = \Psi_{0\eta}, \quad (2.38)$$

$$\theta_{0\eta\eta} - 2\sin\alpha(1-n^2)U_0 U_{0\eta} + \sin\alpha\theta_{0\eta}\Phi_0 + \sin\alpha\Psi_0\theta_0 + 2\sin^2\alpha U_0\theta_0 + (n-1)\xi\{-\sin^2\alpha\theta_0 U_{0\xi} + \sin^2\alpha U_0\theta_{0\xi} + \Psi_{0\xi}U_{0\eta}\} = 0, \quad (2.39)$$

subject to the following boundary conditions:

$$U_0(\xi,0) = \Psi_0(\xi,0) = 0, \quad (2.40)$$

$$\Phi_0(\xi,0) = g(\xi), \quad (2.41)$$

and

$$U_0 \to f(\xi), \quad \theta_0 \to 0 \quad \text{as } \eta \to \infty. \quad (2.42)$$

Here we have assumed that $\Phi_w(\xi,\zeta) \to g(\xi)$ as $\zeta \to \infty$. The above, coupled with symmetry considerations, also implies that as $\eta \to \infty$,

$$\Phi_{0\eta}, \Psi_0 \to f(\xi)\sin\alpha + \tfrac{1}{2}(1-n)\xi\sin\alpha f_\xi. \quad (2.43)$$

If we replace η by $\eta/\sin\alpha$ and Ψ_0 by $\sin\alpha\Psi_0$ (other variables being left unaltered) in the system (2.36)–(2.43) then the $\sin\alpha$ (and hence all α) terms are removed from the system, and hence in the limit of $\zeta \to \infty$, to leading order it is sufficient to consider merely the case $\alpha = 90°$. In Appendix A we show that it is possible to categorize different families of solution in terms of $\theta_{0\eta}(\eta = 0)$, which if $g(\xi) = 0$ gives

$$\theta_{0\eta}(\eta=0) = \sin\alpha\{[nf(\xi) + \tfrac{1}{2}(1-n)\xi f_\xi]^2 - \tfrac{1}{2}\xi f[(1-n^2)f_\xi + \xi(1-n)^2 f_{\xi\xi}]\}. \quad (2.44)$$

The nature of the solutions of the system (2.36)–(2.43) turns out to be of much interest, but a discussion of this will be deferred until later in the paper. However we note that there is some similarity here with the *parabolized Navier–Stokes equations* approach, frequently employed in computational fluid dynamics (see Rubin 1982, for example), although that technique is not strictly a rational procedure, and this is reflected in a number of issues linked to numerical stability (linked to the fact that an elliptic system is treated parabolically); the present scheme, currently under discussion, is a totally rational procedure.

In order to accurately compute the full system (2.23)–(2.26) it is also necessary to compute the next-order terms in the expansions (2.32)–(2.35). This, through straightforward analysis, leads to the conclusion that $U_1 \equiv \Phi_1 \equiv 0$, whilst Ψ_1 and θ_1 are described by

$$\theta_1\sin^2\alpha = \Psi_{1\eta} + \cos\alpha(\Phi_{0\eta} - \Psi_0), \quad (2.45)$$

$$\theta_{1\eta\eta} + \theta_{1\eta}\Phi_0\sin\alpha + \Psi_1\theta_0\sin\alpha - 2\theta_{0\eta}\cos\alpha + 2\eta(n^2-1)\sin\alpha\cos\alpha U_0 U_{0\eta} + (n-1)\xi\{-\theta_1 U_{0\xi}\sin^2\alpha + U_0\theta_{1\xi}\sin^2\alpha + \Phi_{0\xi}U_{0\eta}\cos\alpha + \Psi_{1\xi}U_{0\eta}\} + 2\sin^2\alpha U_0\theta_1 = 0, \quad (2.46)$$

subject to

$$\Psi_1(0,\xi) = -g(\xi)\cos\alpha, \quad (2.47)$$

$$\theta_1 \to 0, \quad \Psi_1 \to \Phi_0 - \eta\Phi_{0\eta} \quad (2.48)$$

as $\eta \to \infty$.

The question of the existence of non-integer powers of ζ arising in the expansions (2.32)–(2.35) was addressed by Pal & Rubin (1971) and DD (no relevant terms were found to exist) and will not be discussed here. In the following section we go on to consider solutions for $U_0(\xi \to 0, \eta), \Phi_0(\xi \to 0, \eta), \Psi_0(\xi \to 0, \eta)$ and $\theta_0(\xi \to 0, \eta)$, i.e. similarity solutions, with emphasis on the effects of wall transpiration.

3. The nature of the similarity solutions with wall transpiration in the limit $\zeta \to \infty$

Here we consider the effect of suction/blowing normal to the wall on the nature of the similarity solutions in the far field (i.e. as $\zeta \to \infty$ with $\xi = 0$, considering the leading-order terms in (2.32)–(2.35)). For this, we consider non-zero values of the transpiration parameter $g(0)$ (see (2.41)), and investigate the effects of varying this parameter and the pressure gradient parameter, n. Note that $g(0) < 0$ corresponds to wall blowing, whilst $g(0) > 0$ implies wall suction, and that we may utilize the aforementioned transformations to enable us to replace α by 90°.

Figure 1(*a–c*) shows the variations of $U_{0\eta}(\eta = 0)$ and $\theta_0(\eta = 0)$ with n, for selected values of $g(0)$. The significance of the dashed and solid lines will be explained in the following section. Note that from DD we certainly expect other solution branches to exist (in particular for negative values of n). The no-transpiration case results are shown in figure 1(*a*) ($g(0) = 0$) and will serve as a reference; two-dimensional results correspond to $n = 0$ and may be identified as the case with $U_{0\eta}(\eta = 0) = \theta_0(\eta = 0)$. For $g(0) = 0$, this is the lower $n = 0$ point in the $U_{0\eta}(\eta = 0)$ distribution and the upper $n = 0$ point in the $\theta_0(\eta = 0)$ distribution.

The effect of increasing $g(0)$ (i.e. suction) is shown in figure 1(*a*). An important particular case seems to be $g(0) = 0.45658$ (approximately), where the nose of the primary solution branch reaches $n = 0$ exactly. Consequently we see that for $g(0) > 0.45658$ (approximately), the two-dimensional point moves from the lower (upper) portion of the $U_{0\eta}(\eta = 0)$ ($\theta_0(\eta = 0)$) curve to the upper (lower) portion. The overall picture may be clarified by inspection of figure 2, showing the variation of $U_{0\eta}(\eta = 0)$ (solid line) and $\theta_0(\eta = 0)$ (dashed line) with $g(0)$ for $n = 0$. This figure clearly shows the coincidence point at $g(0) = 0.45658$ (approximately). The large suction limit of $g(0)$ positive and increasing with $n = 0$ is considered in Appendix B. Finally, with regard to figure 2, we note that it is not possible to obtain reversed flow if $n = 0$, i.e. reversed flow is not possible without an adverse pressure gradient, a conclusion that seems entirely consistent with physical expectation.

Consider now the effect of wall blowing ($g(0) < 0$). As this is increased, the small solution loop close to the origin is seen to expand ($g(0) = -0.44$ in figure 1*b*), whilst a loop appears in the $\theta_0(\eta = 0)$ distribution of the primary solution branch. Increased blowing results in a merger of these two solution branches (close to $g(0) = -0.445$), the hybrid branch terminating at the origin, with a cusp-like behaviour, although as the blowing is increased further, this cusp-like behaviour diminishes (figure 1*c*, $g(0) = -1$). As the blowing is further increased, a marked terminal point, with a cusp, forms at the origin ($g(0) = -1.25$ in figure 1*c*), and this solution branch exists only for $n \geqslant 0$. The metamorphosis of the solution for the important case $n = 0$ is made clearer by inspection of figure 2. From this we see no less than four critical values of $g(0)$, in this case. At all these critical points, the limit is $U_{0\eta}(\eta = 0) = \theta_0(\eta = 0) \to 0$. These points are analysed in some detail in Appendix C, and correspond physically to flows involving massively displaced shear layers, above a region of relatively stagnant

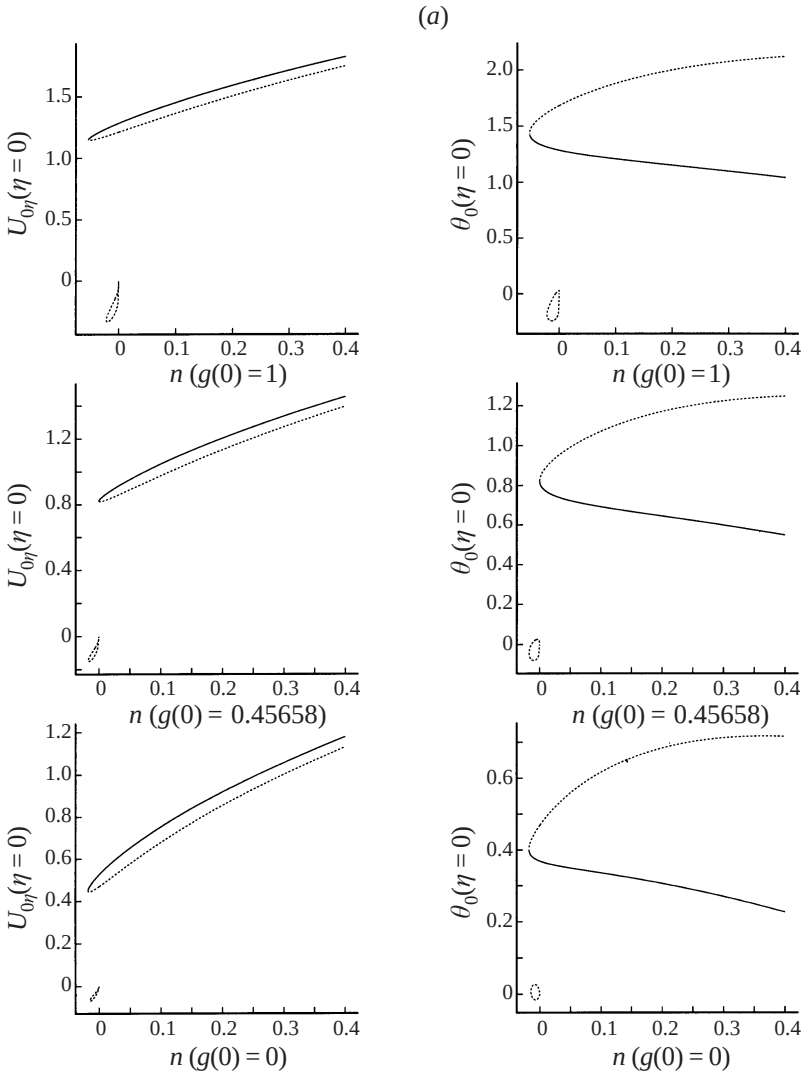

FIGURE 1(*a*). For caption see page 134.

flow lying above the wall; these represent a class of (generally) three-dimensional separated flows.

The small loop close to the origin in the $g(0) = 0$ case appears to be quite a generic feature, with both the upper and lower portions of this solution branch terminating at the origin; indeed, the limiting case for $g(0) = 0$, $n \to 0-$ is analysed in Appendix D, which suggests again a class of flow, including three-dimensional separated flows, which are not unrelated to the flows in the region of the terminus points of figure 2 (discussed in Appendix C).

4. The nature of the non-similarity solutions in the limit $\zeta \to \infty$

In this section we focus our attention on (numerical) solutions to the system (2.36)–(2.43) for cases with no transpiration. In DD it was shown that the behaviour of the similarity solutions in the limit $\zeta \to \infty$ was vital in understanding the existence,

(*b*)

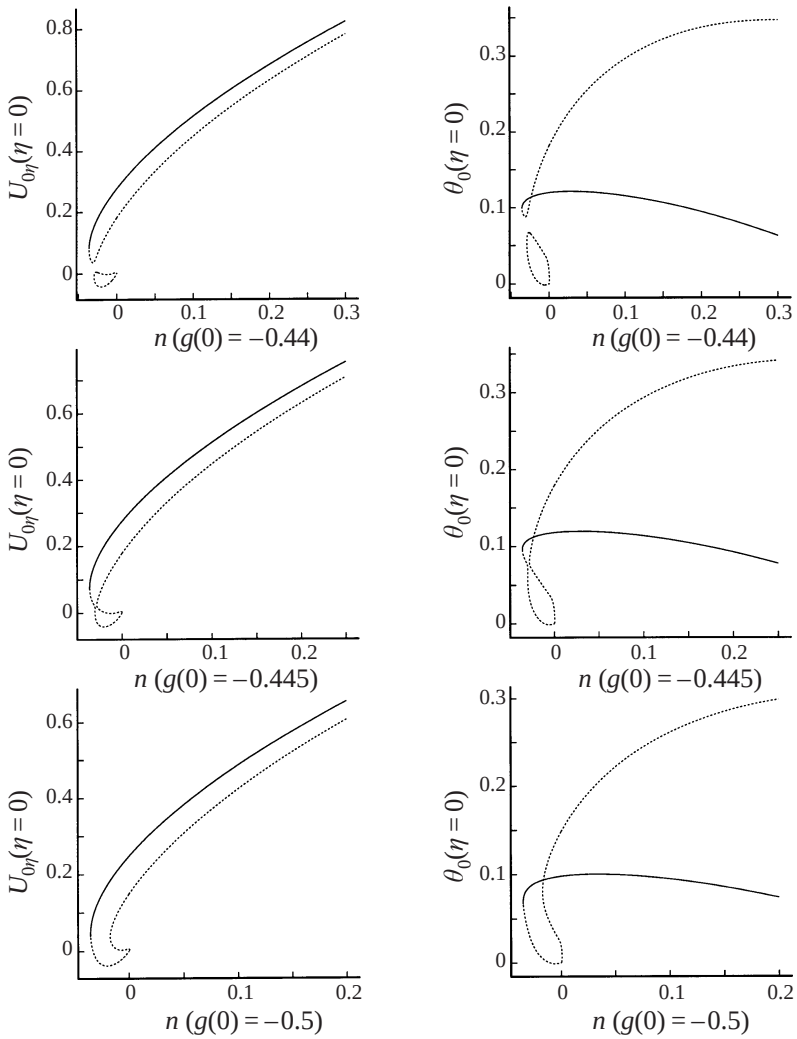

FIGURE 1(*b*). For caption see page 134.

location and nature of solutions, and also in obtaining accurate solutions to the full problem; this is equally true here in the case of non-similarity flows, in which we allow the flow to develop in the streamwise (ξ) direction. In all cases, we take our starting solution (i.e. initial conditions) as computed from (2.36)–(2.43) with $\xi = 0$, which are exactly those solutions computed in DD. Here we shall confine our attention exclusively to the primary solution branch (i.e. the branch that exists for $-0.018\ldots < n < \infty$). Since the system (2.36)–(2.43) is parabolic in ξ, standard numerical practice suggests that starting with the given solution at $\xi = 0$ as the upstream condition, a marching procedure forward in ξ should be appropriate. As noted in § 2, for this aspect of the work we may set $\alpha = 90^\circ$ without any loss of generality.

Standard second-order central differencing in η was employed, together with a Crank–Nicolson procedure in ξ (also of second-order accuracy) and Newton iteration was employed to handle the inherent nonlinearity of the system.

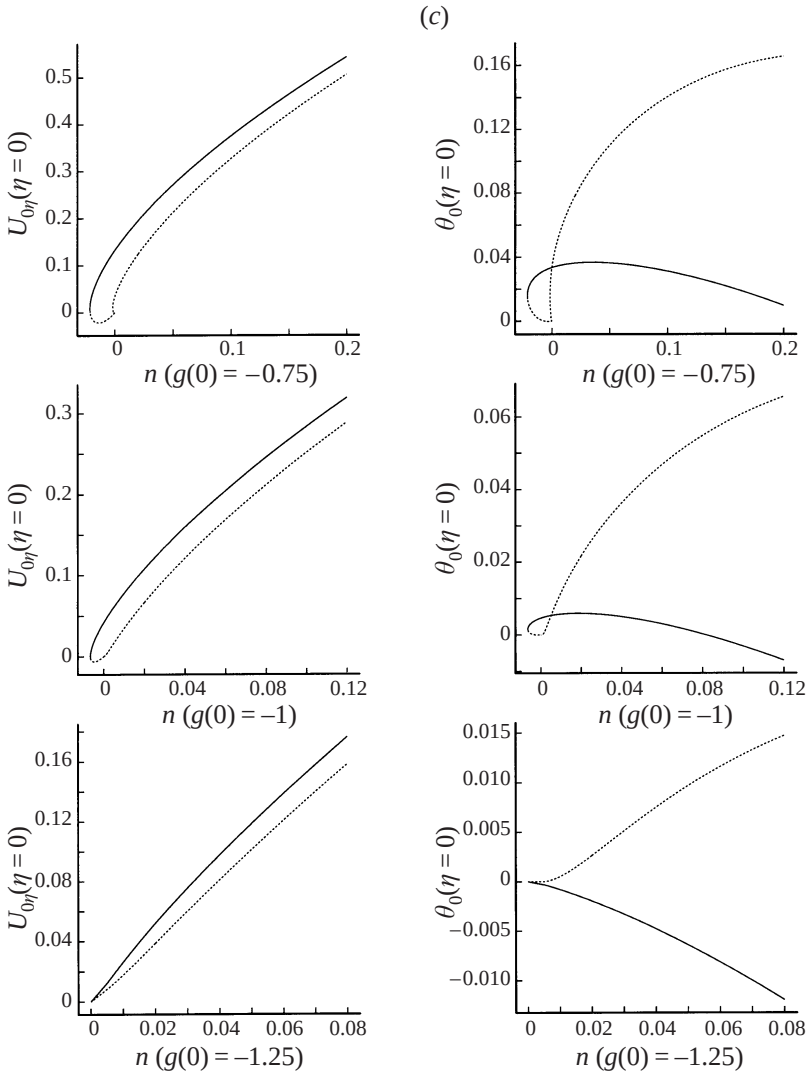

FIGURE 1 (*a–c*). $U_{0\eta}(\eta = 0)$ and $\theta(\eta = 0)$ distributions, varying $n, g(0)$ as indicated.

4.1. *Lower primary* $\theta_0(\eta = 0)$ *solution branch*

We consider, first, initial conditions based on the lower $\theta_0(\eta = 0)$ portion of the primary solution branch. Figure 3(*a*) shows distributions of $U_{0\eta}(\xi, \eta = 0)$, $W_{0\eta}(\xi, \eta = 0)$ and, as a measure of boundary-layer displacement effects, $\delta_0^* = [\Phi_0 - \eta\Psi_0]_{\eta\to\infty}$, for the particular case $n = 0$, with

$$f(\xi) = 2 - \mathrm{e}^{-\xi}. \tag{4.1}$$

This is a model of an accelerating free stream, increasing from unity to two. We are of course quite at liberty to specify the free-stream variation of the streamwise component of the flow. This is equivalent to specifying the pressure gradient in the streamwise direction, which is precisely the procedure followed in classical two-dimensional boundary-layer calculations. Likewise, in practical situations the pressure distribution could be obtained as a result of an outer (inviscid) calculation, or even

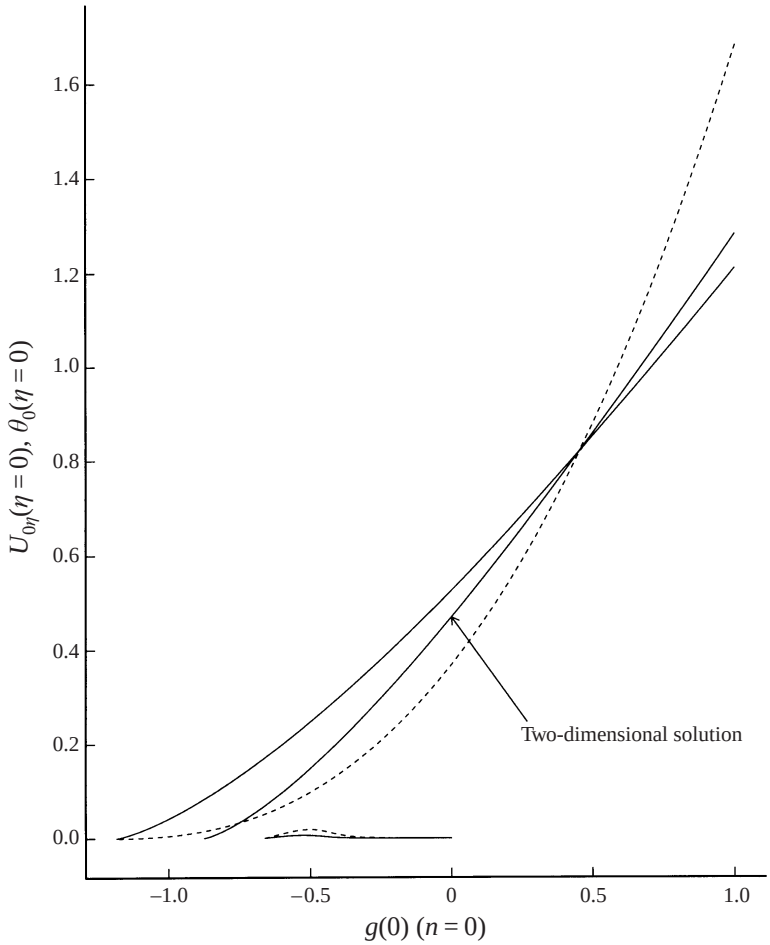

FIGURE 2. $U_{0\eta}(\eta = 0)$ (solid line) and $\theta_0(\eta = 0)$ (dashed line) distributions, varying $g(0)$, $n = 0$. (Note $U_{0\eta}(\eta = 0) = \theta_0(\eta = 0)$ for two-dimensional solution.)

from experimental measurements. It is seen that the solution changes continuously, and the following conditions link downstream to upstream conditions:

$$U_{0\eta}(\xi \to \infty, \eta = 0) \to 2\sqrt{2}U_{0\eta}(\xi = 0, \eta = 0), \tag{4.2}$$

$$W_{0\eta}(\xi \to \infty, \eta = 0) \to 2\sqrt{2}W_{0\eta}(\xi = 0, \eta = 0), \tag{4.3}$$

$$\delta_0^*(\xi \to \infty) \to \sqrt{2}\delta_0^*(\xi = 0), \tag{4.4}$$

results that can be inferred from the governing equations (2.36)–(2.43) by replacing $f = 1$ by $f = 2$, and rescaling. Therefore the flow accelerates from one state on the lower $\theta_0(\eta = 0)$ portion of the solution branch to the corresponding (i.e. scaled) point on the same solution branch. In this case there was no evidence of a transition between solution branches; indeed this was a feature common in all computations emanating from the lower of the solution branches.

Figure 3(*b*) shows the same free-stream development as in figure 3(*a*), but with $n = 0.35$; again conditions (4.2)–(4.4) are seen to hold, indicating that this solution

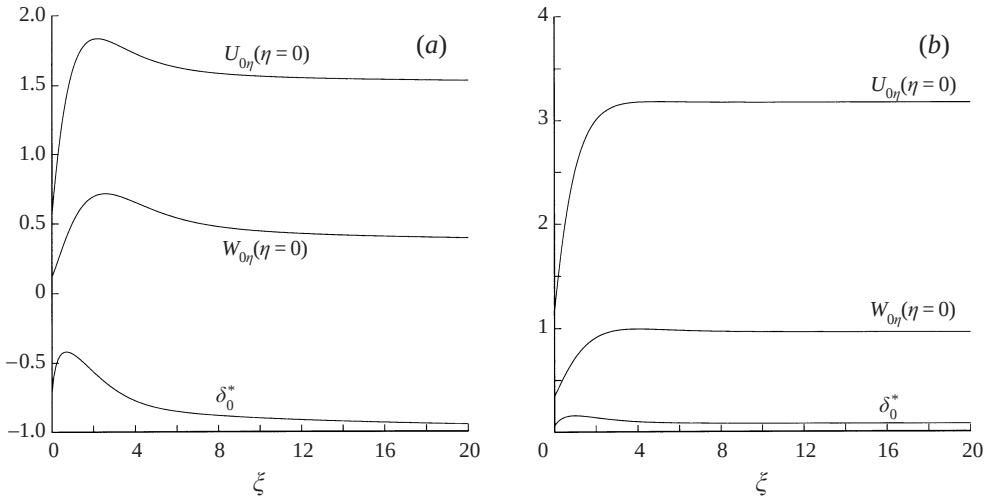

FIGURE 3. Streamwise development of $\zeta \to \infty$ solution, (*a*) $n = 0$ and (*b*) $n = 0.35$, lower solution, $f(\xi) = 2 - \mathrm{e}^{-\xi}$.

also remains on the lower portion of the solution branch; indeed we have not been able to find examples where a lower-branch solution ends up on the upper-solution branch.

One aspect of the results worth noting is that in spite of the rapid exponential asymptote of (4.1) as ξ increases, this is not mirrored in the quantities shown in figure 3(*a*, *b*), inspection of which suggests a likely algebraic asymptote in this limit; this effect is perhaps more marked in the $n = 0$ case shown in figure 3(*a*). An explanation for this is as follows (cf. Libby & Fox 1963): suppose the basic state denoted by subscript 00 below has perturbation eigensolutions. In particular (assuming $\mathrm{Re}\{\lambda\} < 0$) as $\xi \to \infty$ let

$$U_0(\xi, \eta) = U_{00}(\eta) + \xi^{\lambda}\tilde{u} + \cdots, \tag{4.5}$$

$$\Phi_0(\xi, \eta) = \Phi_{00}(\eta) + \xi^{\lambda}\tilde{\phi} + \cdots, \tag{4.6}$$

$$\Psi_0(\xi, \eta) = \Psi_{00}(\eta) + \xi^{\lambda}\tilde{\psi} + \cdots, \tag{4.7}$$

$$\theta_0(\xi, \eta) = \theta_{00}(\eta) + \xi^{\lambda}\tilde{\theta} + \cdots\ . \tag{4.8}$$

Substitution of these expansions into (2.36)–(2.43) leads to the following set of perturbation equations:

$$2\tilde{u} + (1-n)\lambda\tilde{u} = \tilde{\phi}_{\eta} + \tilde{\psi}, \tag{4.9}$$

$$\tilde{u}_{\eta\eta} = 4nU_{00}\tilde{u} + \lambda(1-n)U_{00}\tilde{u} - \tilde{\phi}U_{00\eta} - \tilde{u}_{\eta}\Phi_{00}, \tag{4.10}$$

$$\tilde{\theta} = \tilde{\psi}_{\eta}, \tag{4.11}$$

$$\tilde{\theta}_{\eta\eta} - 2(1-n^2)\left[U_{00}\tilde{u}_{\eta} + \tilde{u}U_{00\eta}\right] + \tilde{\theta}_{\eta}\Phi_{00} + \theta_{00\eta}\tilde{\phi} + \tilde{\psi}\theta_{00} + 2\tilde{u}\theta_{00} + \Psi_{00}\tilde{\theta} + 2U_{00}\tilde{\theta} + (n-1)\lambda\{-\theta_{00}\tilde{u} + U_{00}\tilde{\theta} + \tilde{\psi}U_{00\eta}\} = 0, \tag{4.12}$$

subject to the boundary conditions

$$\tilde{u}(0) = \tilde{\phi}(0) = \tilde{\psi}(0) = 0, \tag{4.13}$$

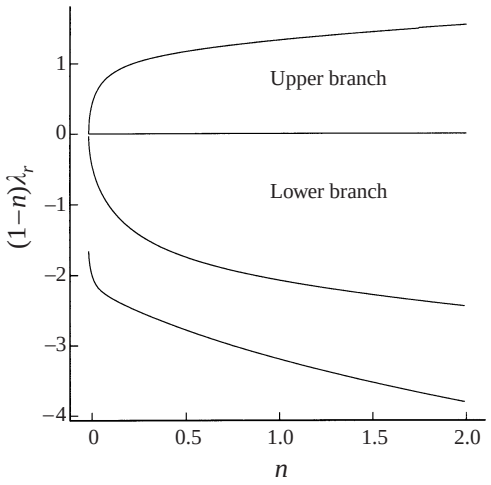

FIGURE 4. Variation of eigenvalues with n.

$$\tilde{u}, \tilde{\psi}, \tilde{\theta} \to 0 \quad \text{as } \eta \to \infty. \tag{4.14}$$

We take $U_{00}(\eta) = U_0(\xi = 0, \eta), \Phi_{00}(\eta) = \Phi_0(\xi = 0, \eta), \Psi_{00}(\eta) = \Psi_0(\xi = 0, \eta)$ and $\theta_{00}(\eta) = \theta_0(\xi = 0, \eta)$, i.e. the similarity solutions presented in DD (although these are strictly far-downstream values, we have seen that in the above these are merely scaled functions of the leading-edge solutions if $f(\xi) \to$ constant as $\xi \to \infty$).

The system (4.9)–(4.14) was tackled using two independent approaches. In the first, the system was approximated by second-order finite differences, and the complete algebraic eigenvalue problem was solved using a QZ algorithm. In the second, a local search scheme based on Runge–Kutta methods was implemented. Frequently the former method was used to provide starting estimates for the latter (more accurate) method. The real parts of the eigenvalues are shown in figure 4. The region marked 'lower branch' corresponds to $(1 - n)\lambda_r < 0$, where $\lambda_r = \mathrm{Re}\{\lambda\}$ (the upper branch results will be discussed below). Here it is appropriate to study $(1 - n)\lambda_r$, which is physically more meaningful in terms of the downstream development of the solution in physical (i.e. x) space, rather than computational (i.e. ξ) space. It is found that in the range of n shown: (i) there are many (almost certainly an infinite number) real modes, all with $\mathrm{Re}\{(1 - n)\lambda\} < 0$; in figure 4 we have just shown the first two modes of smallest magnitude, (ii) at the lowest value of the range of n for which this family of solutions exists ($n \approx -0.018$), the eigenvalue with smallest magnitude approaches zero. Note that the eigenvalue of smallest magnitude will be primarily responsible for controlling the downstream flow behaviour. These results go some way in explaining the slow, algebraic decay encountered downstream, especially in the case of $n = 0$ (figure 3*a*) for which we see that the first eigenvalue $|\lambda|$ is quite small. These results do raise questions about the limit as $n \to -0.018$ (approximately), but these will be deferred until later.

We now turn our attention to the case

$$f(\xi) = 2\mathrm{e}^{-\xi} - 1. \tag{4.15}$$

Again, our comments regarding (4.1) are applicable, namely that this is a model free-stream variation (which we are at liberty to specify), (4.15) representing a decelerating flow. Figure 5(*a*) shows results for the case $n = 0.35$. The flow is seen to reach a reversal point at which $U_{0\eta}(\eta = 0) = 0$ at $\xi \approx 0.42$. Figure 5(*b*) shows the

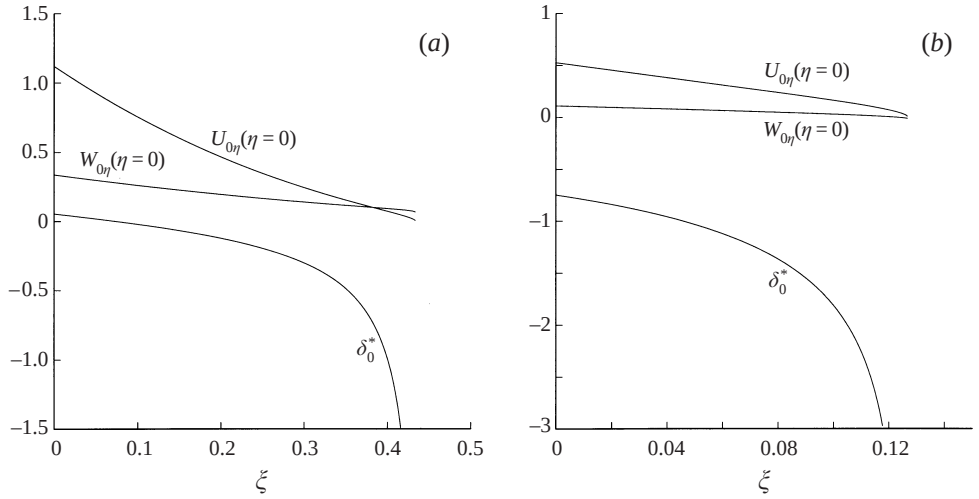

FIGURE 5. Streamwise development of $\zeta \to \infty$ solution, (*a*) $n = 0.35$ and (*b*) $n = 0$, lower solution, $f(\xi) = 2e^{-\xi} - 1$.

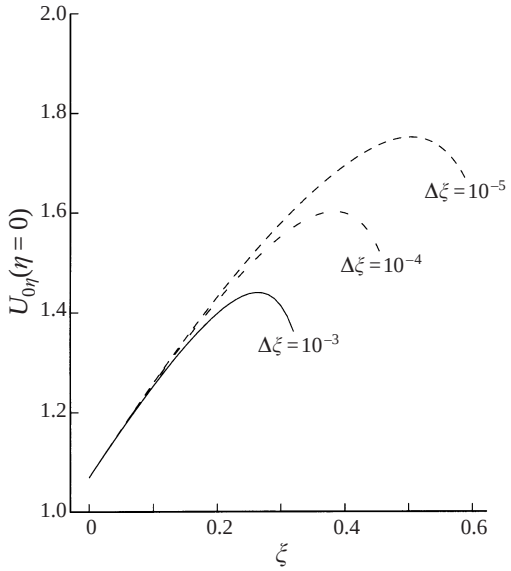

FIGURE 6. Streamwise development of $U_{0\eta}(\eta = 0)$ ($\zeta \to \infty$ solution), $n = 0.35$ upper solution.

corresponding results for $n = 0$; in this case, flow reversal occurs at $\xi \approx 0.12$. All the computed quantities (including those in figure 5*b*) suggested that flow reversal occurs in a singular fashion, culminating with a Goldstein (1948) singularity, as is always encountered in analogous two-dimensional computations of separating boundary layers with prescribed (adverse) pressure gradients. In this respect we have that $U_{0\eta}(\eta = 0) = O((\xi_s - \xi)^{1/2})$ as the separation point ξ_s is approached; our numerical results were entirely consistent with this behaviour. As with fully two-dimensional flows, it is not possible or appropriate to extend these calculations past ξ_s.

4.2. *Upper* $\theta_0(\eta = 0)$ *solution branch*

Computations for an accelerating flow, with $f(\xi)$ described by (4.1) and $n = 0.35$ (upper $\theta_0(\eta = 0)$ solution branch) are shown in figure 6, where we present results for $U_{0\eta}(\eta = 0)$. These results were all obtained using a transverse grid $\Delta\eta = 0.025$, extending out to $\eta_\infty = 160$ (a much finer and more extensive grid than necessary for any of the lower solution branch computations discussed above). As indicated in the figures, three grids in ξ were taken, namely $\Delta\xi = 10^{-3}, 10^{-4}$ and 10^{-5}, again all much smaller than necessary for any of the lower-branch solutions described previously. In spite of the smallness of these $\Delta\xi$, we see a drastic variation in solutions as $\Delta\xi$ varies. Variation of other numerical parameters produced similar spectacular changes in solution, and other computed quantities (including $W_{0\eta}(\eta = 0)$ and δ_0^*) exhibited similar behaviours to the streamwise wall shear stress. In all cases, all the indications were that these difficulties emanated from the leading edge (i.e. $\xi = 0$).

In order to explain these difficulties, we re-consider the expansions (4.5)–(4.8), but this time instead consider the limit $\xi \to 0$, and consequently we seek eigenvalues for which $\mathrm{Re}\{(1-n)\lambda\} > 0$. The system (4.9)–(4.12) was then re-investigated, using precisely the same numerical procedures as above, but rather focusing attention on the upper portion of the primary solution branch. Results for $\mathrm{Re}\{(1-n)\lambda\}$ are shown in figure 4 in the region marked 'upper branch' and corresponds to the region $(1-n)\lambda_r > 0$. The following general features were observed: (i) on this solution branch, a single, real, positive $(1-n)\lambda$ was found to exist; (ii) the genesis of this particular eigenvalue occurred at $n = -0.018$ (approximately), i.e. at the lowest extremum of the solution branch; (iii) many (probably an infinity of) real, negative $(1-n)\lambda$ were also found to exist. Interestingly, the single positive eigenvalue connects to the downstream root with smallest magnitude (which is primarily responsible for controlling the downstream asymptote of the solution), as discussed above. We note that the particular result for λ for the case of Blasius flow ($n = 0$) agrees precisely with the result of Luchini (1996) in his study of the spatial (steady) stability of the Blasius boundary layer; in particular he proposed his solution as a candidate for an initial linear mechanism that leads to bypass transition. That work would also seem to have some link to the response of Blasius boundary layers to free-stream vorticity (Bertolotti 1997; Bertolotti & Kendall 1997).

The reason for the difficulties faced in the computation of the upper-branch family of solutions is now clear, namely the occurrence of these leading-edge eigensolutions which render any marching process non-unique/ill-posed. Indeed, in spite of the parabolic nature of the equations, the problem must contain some 'upstream influence', i.e. the far downstream nature of the flow affects the flow upstream. Note that this is somewhat different from the situation encountered in pseudo-parabolic problems (see Phillips 1996, for example), where sign changes in coefficients of the differential equation lead to type changes of the differential equation. This is not the situation here (certainly if the flow is not reversed). A strongly analogous situation is found in the computation of certain two-dimensional hypersonic boundary layer problems (Neiland 1970; Mikhailov, Neiland & Sychev 1971 and Brown & Stewartson 1975), where some similar characteristics for the results for leading-edge eigenvalues are also found. We can now reveal the significance of the broken and solid lines in our similarity, transpiration results presented in figure 1(*a–c*). Here, solid lines correspond to regimes where only negative values of $(1-n)\lambda_r$ exist, and thus standard parabolic marching techniques may in principle be used in progressing the solution away from these similarity forms; dashed lines refer to flow profiles which exhibit positive

$(1-n)\lambda_r$. In general, for all values of suction and blowing, it appears that there is at most one solution which has $\mathrm{Re}\{\lambda(1-n)\} < 0$ for all eigenvalues for a given value of n. Further, generally, the solution with the largest $U_{0\eta}(\eta = 0)$ corresponds to the branch without positive $(1-n)\lambda_r$. In certain, limited, regions of parameter space, multiple eigenvalues with positive real part were observed, and also complex eigenvalues were occasionally found. Further, our numerical results strongly suggested that the change in the nature of the smallest eigenvalue from positive to negative real part always occurs at an extreme value of n.

The question then becomes whether it is possible, in spite of these difficulties, to perform calculations of this type, on the upper family branch; the answer turns out to be affirmative. There are some similarities with those found in interacting boundary layers involving upstream eigensolutions. In the past, two approaches have been developed for such problems. The first involves the adjustment of a (single) unknown upstream coefficient, in order to produce the appropriate downstream response (Stewartson & Williams 1969). This is usually undertaken as a trial-and-error approach, although it has been very effectively used in a number of different problems. The second approach has been to treat the problem as if it were partially elliptic, coupling the upstream and downstream behaviours, in order to avoid the unbounded downstream growth of eigensolutions; this type of method was adopted by Rizzetta, Burggraf & Jenson (1978). In the present context the latter type of approach appears to be the more attractive, in so far as it seems likely that the trial-and-error approach would prove highly sensitive and could easily lead to numerical complications. The disadvantage with the 'quasi-elliptic' approach is the much more substantial demands on computational resources, particularly in terms of memory requirements; however what turns out to be the robustness of this approach offsets this disadvantage.

The technique applied was to treat (2.36)–(2.39) using standard second-order central differencing in both η and ξ. Early attempts at using line relaxation methods on the algebraic system (in both the η- and ξ-directions) proved unsuccessful, and so instead a Newton iteration scheme solving for all grid points simultaneously was adopted. If N_ξ and N_η denote the number of grid points in the ξ- and η-directions, respectively, then the resulting system of equations can be written in banded form, symbolically

$$\boldsymbol{A} \cdot \delta \boldsymbol{X} = \boldsymbol{B}, \tag{4.16}$$

where $\boldsymbol{A}$ is a banded array of width $16N_\xi$ or $16N_\eta$ (the choice being the smaller of the two) by $4N_\xi N_\eta$ long, $\delta \boldsymbol{X}$ is the vector of the increments of the computed function and $\boldsymbol{B}$ a column vector of length $4N_\xi N_\eta$. The sparseness of this system was fully exploited.

One further point remains, namely the imposition (and nature) of the downstream boundary conditions. From the point of view of freestream variations described by (4.1) (and other forms for which $f(\xi) \to$ constant as $\xi \to \infty$) it is clear that the downstream form will certainly admit similarity-type solutions. (This will also be true for more general forms of $f(\xi)$, such as those involving algebraic behaviours downstream, although the situation would be somewhat more complicated on account of the different form of the similarity solution to that at the leading edge; these cases are slightly more complicated, but conceptually the same.) One obvious procedure would appear to be to impose the similarity solution corresponding to $f(\xi \to \infty)$. An alternative to this, for classes of $f(\xi)$ of type (4.1) (and this was our preferred method), is to impose the zero streamwise derivative (Neumann) condition on all the computed quantities (namely U_0, Φ_0, Ψ_0 and θ_0). This seemed to reduce the domain

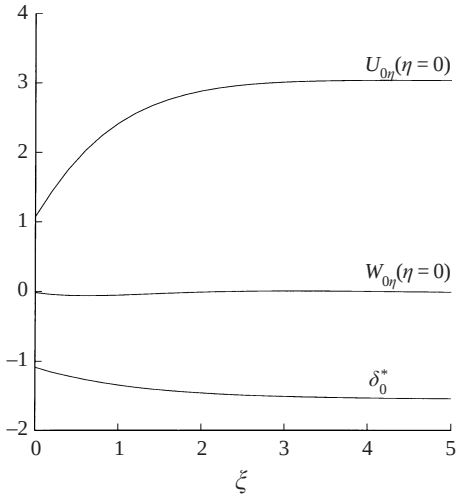

FIGURE 7. Streamwise development of $\zeta \to \infty$ solution, $n = 0.35$ upper $\theta_0(\eta - 0)$ solution at $\xi = 0$, $f(\xi) = 2 - e^{-\xi}$ (global solution scheme).

truncation errors somewhat, compared with specifying flow quantities *per se*, and is entirely consistent with the imposition of a similarity solution downstream of the same form as that at the leading edge (where we imposed a solution derived directly from the similarity set of equations).

Figure 7 shows streamwise variations of $U_{0\eta}(\eta = 0)$, $W_{0\eta}(\eta = 0)$ and δ_0^*, with ξ, for $f(\xi)$ given by (4.1) and $n = 0.35$, computed using the global procedure involving (4.16); note that this is identical to the problem considered unsuccessfully previously, using marching procedures, the results of which were shown in figure 6. In this case a smooth transition from the leading-edge state to the far-downstream state is clearly observed, with the far-downstream solution linked to the leading-edge solution through (4.2)–(4.4), again. (Incidentally we found that our global technique was applicable to lower-branch solutions, although this is clearly a much less efficient treatment of the problem than standard marching procedures.) A typical computation involved 101 grid points in the transverse (η) direction, extending out to $\eta \approx 10$, and 61 points in the streamwise (ξ) direction, extending to $\xi = 5$ or 10; the results shown in figure 7 are graphically accurate (with an accuracy of typically 2%).

A number of numerical experiments were performed to investigate whether it is possible to have a smooth transition from the upper $\theta_0(\eta = 0)$ state at $\xi = 0$ to the lower $\theta_0(\eta = 0)$ state far downstream; no acceptable solutions of this type were found, suggesting that such solutions are not possible.

5. The full problem

In computing the full problem, we choose to use working variables that (i) remain bounded as η and/or $\zeta \to \infty$, and (ii) retain the useful symmetry properties about the corner bisector plane (in the case of symmetrical flows), which thus enables us to halve the computational domain. To this end we retain the use of the $U(\xi, \eta, \zeta)$ variable, but replace the three other dependent variables by the following 'tilde' variables:

$$\Phi(\xi, \eta, \zeta) = \eta \Psi_0(\xi, \zeta) + \tilde{\Phi}(\xi, \eta, \zeta), \tag{5.1}$$

$$\Psi(\xi,\eta,\zeta) = \zeta\Psi_0(\xi,\eta) + \tilde{\Psi}(\xi,\eta,\zeta), \tag{5.2}$$

$$\theta(\xi,\eta,\zeta) = \zeta\theta_0(\xi,\eta) - \eta\theta_0(\xi,\zeta) + \tilde{\theta}(\xi,\eta,\zeta). \tag{5.3}$$

The governing equations for the tilde variables are not given here in the interests of brevity, but are readily derivable from (2.23)–(2.29). It was noted in DD that accurate domain truncation was essential for meaningful numerical results, and to this end (2.32)–(2.35) must be treated appropriately. Setting $U(\xi,\eta,\zeta\to\infty)\to U_0(\xi,\eta)$ and $\tilde{\Phi}(\xi,\eta,\zeta\to\infty)\to\Phi_0(\xi,\eta)-\eta\Psi_0(\xi,\zeta\to\infty)$ turns out to be adequate (with a domain truncation error of $O(\zeta^{-2})$), but the $O(\zeta^{-1})$ terms in (2.34) and (2.35) can be numerically significant. For this reason, using the technique employed in DD, the following conditions were placed on $\tilde{\Psi}$ and $\tilde{\theta}$ as $\zeta\to\infty$:

$$\frac{\partial}{\partial\zeta}[\zeta\tilde{\Psi}(\xi,\eta,\zeta)]_{\zeta\to\infty}\to\Psi_1(\xi,\eta), \tag{5.4}$$

$$\frac{\partial}{\partial\zeta}[\zeta\tilde{\theta}(\xi,\eta,\zeta)]_{\zeta\to\infty}\to\theta_1(\xi,\eta), \tag{5.5}$$

leading to a domain truncation error of $O(\zeta^{-2})$, which turns out to be entirely satisfactory. Two important rationales for having studied the $\zeta\to\infty$ asymptotes can now be clearly seen. This enables us to subtract out the unbounded elements of the solution as η and/or $\zeta\to\infty$ (see (5.1)–(5.3)), and also determines the boundary conditions (5.4), (5.5) for the tilde variables as $\zeta\to\infty$.

In the numerical treatment of the equations for $U,\tilde{\Phi},\tilde{\Psi}$ and $\tilde{\theta}$ arising from (2.23)–(2.29), standard second-order central differencing was used in η and ζ, whilst in the ξ-direction a fully implicit second-order Crank–Nicolson difference scheme was applied. The computational task involved in determining solutions corresponding to the upper solution branch even in the limit as $\zeta\to\infty$ was seen in §4 to be not insubstantial, and it is to be anticipated that a numerical treatment of the full system in this region is currently prohibitive, although the general, global solution procedure devised in §4 could, in principle, be extended to the full problem, given sufficient computational resources. Consequently in all cases below, we shall confine our attention to the lower $\theta_0(\eta=0)$ portion of the primary solution branch, for which, as shown in §4, conventional parabolic marching schemes are generally applicable. Line relaxation was applied to solve the algebraic system of equations at each ξ station. Typical computations using a 201×201 grid in η and ζ, with a grid size of 0.1×0.1, a streamwise grid size of $\Delta\xi=0.01$ and with the symmetry condition invoked along the plane $\eta=\zeta$ typically took 3–4 days on a DEC Alpha 500/500 workstation (or about 2 weeks on a Pentium 90).

Figures 8(a) and 8(b) display results for the case $n=0.35$ (lower branch, in accord with our remarks above), $\alpha=90^\circ$, with a favourable pressure gradient corresponding to (4.1). As expected, both the streamwise wall shear ($\tau=U_\eta(\eta=0)$) and crossflow shear stress ($W_\eta(\eta=0)$) are seen to asymptote downstream to a (scaled) similarity form, in line with (4.2)–(4.4). We note, however, that the ζ-coordinate needs also to be scaled by a factor $\sqrt{2}$ in this limit. Note too that the flow in the immediate vicinity of the wall ($\eta=0$) is directed entirely away from the corner apex.

As an example of a non-90° corner angle case, consider $\alpha=45^\circ$, $n=0.35$. Figure 9(a,b) shows distributions for $\tau=U_\eta(\eta=0)=\sqrt{2}U_{\eta^*}(\eta^*=0)$ and $W_{\eta^*}(\eta^*=0)$ respectively, and again we see the downstream form linked to the leading-edge state through (4.2)–(4.4) (together with the $\sqrt{2}$ scaling on ζ; similarity solutions for $\alpha\neq90^\circ$ have been obtained by Abdulwanis 1997). We note a general reduction in the

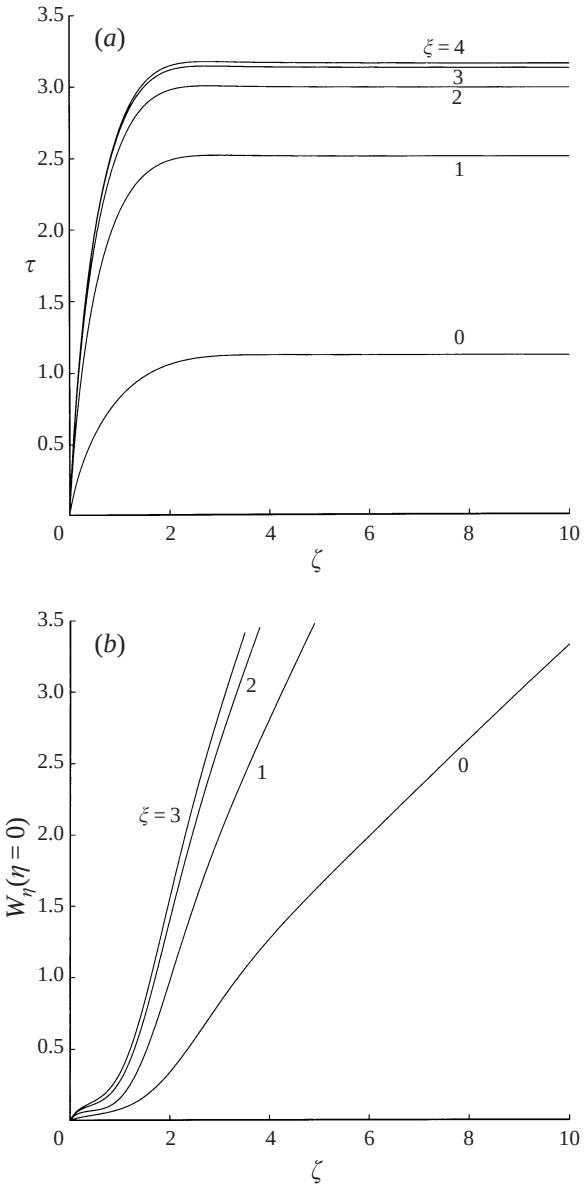

FIGURE 8. (*a*) τ distributions and (*b*) $W_\eta(\eta = 0)$ distributions, full problem, $n = 0.35$ (lower branch), $\alpha = 90°$, $f(\xi) = 2 - e^{-\xi}$.

magnitude of the streamwise shear stress, compared with the corresponding $\alpha = 90°$ case of figure 8, indicating again that the flow close to the wall is directed away from the apex. Figure 9(*c*) shows the secondary velocity vectors in the plane $\xi = 0$, i.e. the similarity solution at the leading edge. It is seen that although, as noted above, the flow near the walls is directed away from the corner apex, closer to the corner bisector line this is not always the case, and it is instead directed towards the apex at distances sufficiently distant from the apex; closer to the corner, the flow is directed entirely away from the apex. Figure 9(*c–g*) shows secondary velocity vectors at stations progressively further downstream, and depict the development of the solution; the

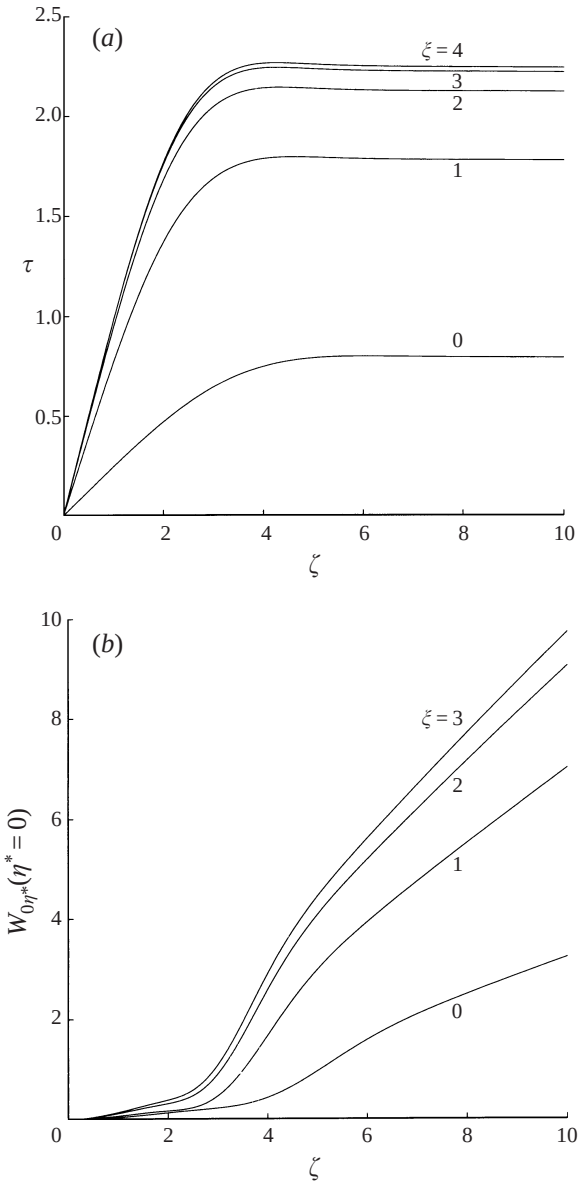

FIGURE 9(*a*, *b*). For caption see facing page.

thinning of the corner region (by the $1/\sqrt{2}$ mentioned noted above) is quite noticeable in these distributions. The overall flow features are retained throughout the transition of the flow between the leading-edge and downstream states. In figure 9(*h*) we show the secondary velocity vectors for the other similarity solution, corresponding to the upper $\theta_0(\eta = 0)$ solution (to re-iterate, it is impractical to compute non-similarity solutions originating from this solution, due to the limitations discussed above). This figure is to be compared directly with figure 9(*c*). In the case of this second similarity solution, we see that the flow in the vicinity of the walls is not unidirectional, but directed towards the apex for $\zeta^* > 5.5$ approximately (recall (2.22) for the link between ζ^* and ζ when $\alpha \neq 90°$), and away from the apex for ζ^* less than this value. Closer to

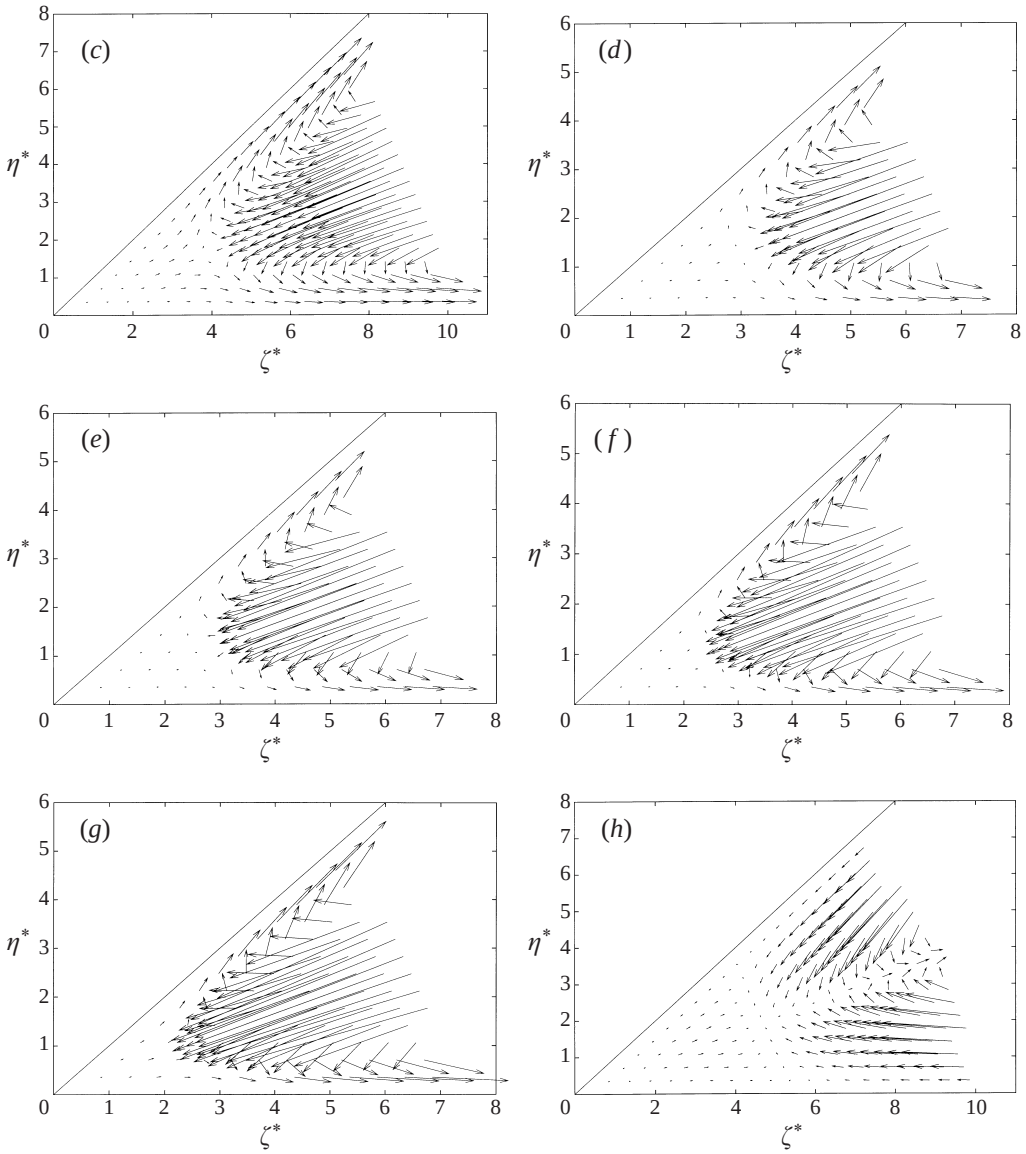

FIGURE 9. (*a*) τ distributions and (*b*) $W_{\eta^*}(\eta = 0)$ distributions, full problem, $n = 0.35$ (lower branch), $\alpha = 45°$, $f(\xi) = 2 - \mathrm{e}^{-\xi}$. (*c–g*) Secondary velocity vectors, $n = 0.35$ (lower branch), $\alpha = 45°$, $f(\xi) = 2 - \mathrm{e}^{-\xi}$: (*c*) $\xi = 0$ (similarity solution), (*d*) $\xi = 0.25$, (*e*) $\xi = 0.5$, (*f*) $\xi = 1.0$, (*g*) $\xi = 2.0$. (*h*) $n = 0.35$ (upper branch), $\alpha = 45°$, $\xi = 0$ (similarity solution).

the corner bisector line the flow is entirely directed away from the apex. We therefore see that the two similarity solutions are quite distinct with regard to the secondary velocity field.

We next turn to an example involving an adverse pressure gradient, specifically $n = 0.35$ (lower branch), $\alpha = 90°$, with the free-stream velocity function $f(\xi) = \mathrm{e}^{-\xi}$. Results for this case are shown in figures 10(*a*) ($\tau = U_\eta(\eta = 0)$) and 10(*b*) ($W_\eta(\eta = 0)$). We note here that strictly, results become invalid if $U(\xi, \eta, \zeta) < 0$, which first occurs in this case just after $\xi = 1.2$. Importantly, we note that (i) all the indications are

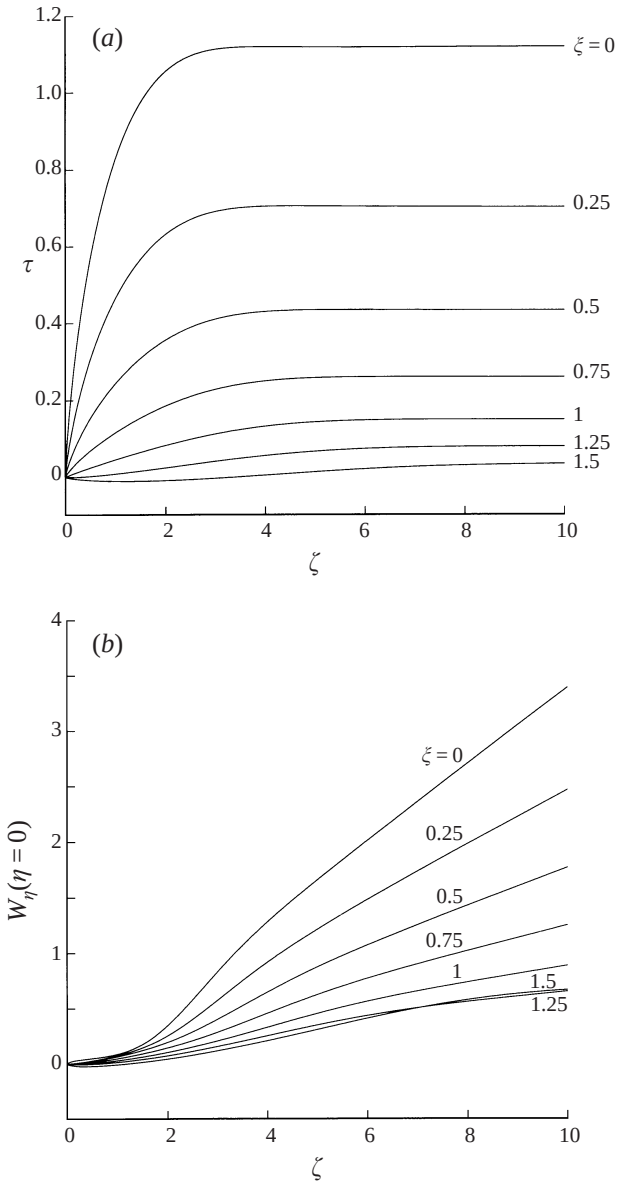

FIGURE 10(*a*, *b*). For caption see facing page.

that flow reversal (at least close to the apex) occurs in a completely regular fashion, and (ii) flow reversal occurs earlier than in the $\zeta \to \infty$ limit, in particular this seems to occur in the immediate vicinity of the corner itself. Figure 10(*c*) shows the vector plots of $(U_\eta(\eta = 0), W_\eta(\eta = 0))$ up to (and just beyond) flow reversal, and illustrates the general transport of fluid (near the wall) away from the corner, particularly as flow reversal occurs. We note that in this case, however, further downstream, close to the corner, a small region exists wherein the flow is directed towards the corner, albeit of small magnitude.

Figures 11(*a*) (τ distribution) and 11(*b*) ($W_\eta(\eta = 0)$ distribution) show results for $n = 0$ (lower branch solution), all other parameters being as in figure 10. Again flow

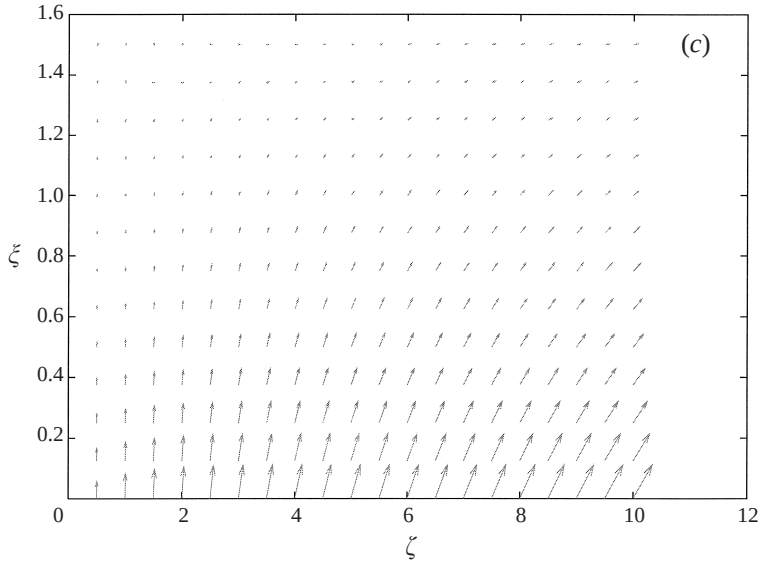

FIGURE 10. (*a*) τ distributions and (*b*) $W_\eta(\eta = 0)$ distributions, full problem, $n = 0.35$ (lower branch), $\alpha = 90°$, $f(\xi) = \mathrm{e}^{-\xi}$. (*c*) Vector plot of $(U_\eta(\eta = 0), W_\eta(\eta = 0))$, full problem, $n = 0.35$ (lower branch).

reversal sets in earlier in this full problem compared with the asymptotic $\zeta \to \infty$ problem studied in §4, and again all the indications are that flow reversal quite regularly but much sooner than in the previous ($n = 0.35$) case, at just after $\xi = 0.06$. This suggests, as we expect, that a favourable pressure gradient delays occurrence of flow reversal in corner flows. In this case the bulk of the fluid close to the wall is directed away from the apex, although in the vicinity of the apex the flow is directed towards the corner; this effect is seen all the way from the leading edge to the flow separation point.

6. Conclusions

In this paper we have extended the work of DD to include consideration of non-90° corner angles, wall transpiration and, perhaps more importantly, non-similarity solutions. The formulation is quite general, and is applicable to obtuse as well as acute corner angles. The numerical results of §3 coupled with the theoretical/asymptotic results in the Appendices gives some rare insight into the nature of grossly separated three-dimensional flows, and confirms the existence of non-unique solutions, so often encountered in this class of flow. These flows are quite generic in nature, involving displaced shear layers above a region of relatively stagnant flow.

The existence of the leading-edge eigensolutions in a number of flow regimes has serious repercussions for boundary-layer calculations of this type. They significantly intensify the computational efforts in the numerical task and lead to prohibitive requirements on computational resources in the case of the fully three-dimensional problem, even with the modern generation of computer hardware. Our analysis demonstrates the nature of the difficulty in the limiting, $|\zeta| \gg 1$, regime, but the same holds with regard to the full computation. The question as to which of the various non-unique solutions would be observed in practice remains to be settled.

A further important observation is that here three-dimensionality appears to alle-

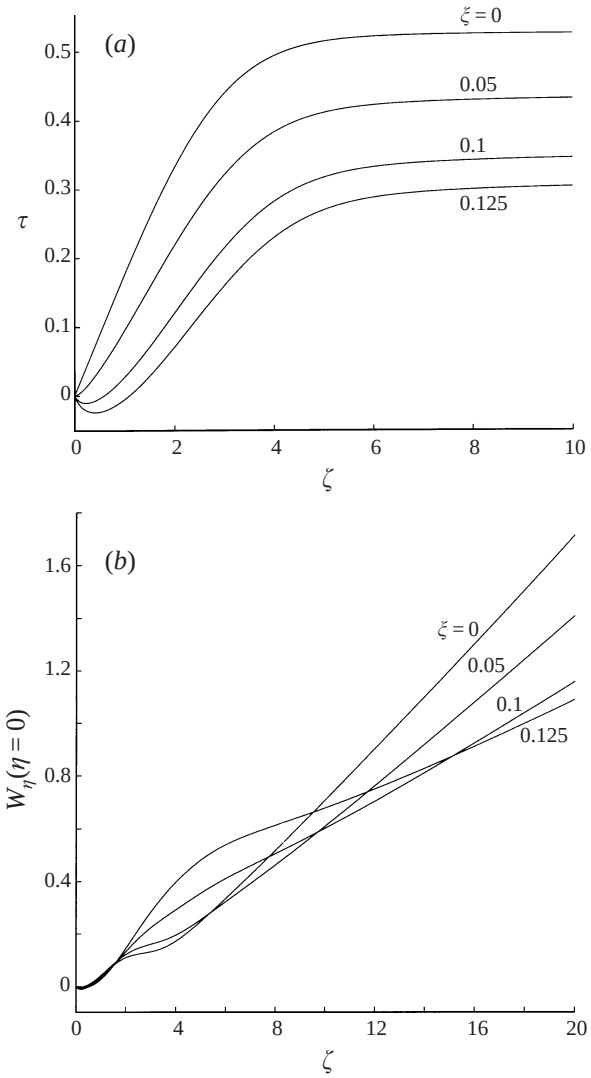

FIGURE 11. (*a*) τ distributions and (*b*) $W_\eta(\eta = 0)$ distributions, $n = 0$ (lower branch), $\alpha = 90°$, $f(\xi) = e^{-\xi}$.

viate the classical two-dimensional Goldstein (1948) singularity, which is always encountered at flow separations (when the streamwise pressure gradient is prescribed), but which our numerical results seem to suggest is avoided, at least in the immediate vicinity of the apex of the corner (but not at large distances from the corner). We note that in the cases tackled (and we have no reason to doubt that these effects are quite generic), the onset of flow reversal can be significantly hastened by a reduction in the value of the pressure gradient parameter *n*.

The present paper also highlights still further explanations for the difficulties in the observation of stable, laminar, similarity, corner-type boundary layers, as noted by Zamir (1981). DD (and confirmed here) found that the main, attached solution branch only exists for $n > -0.018$ (approximately), suggesting that a very small adverse pressure gradient could easily lead to a pressure gradient parameter less than this critical value, thereby disrupting the similarity solution completely; indeed Zamir

(1981) reports on the difficulties with leading-edge effects and with achieving zero pressure gradient flows. The work of DD also reveals that even slight asymmetries to the problem can also cause significant disruptions to the flow (including major changes to the critical value of n above which attached solutions exist); such effects could easily be induced by slight asymmetry/misalignment in the experiments. Further still, it is suggested from the work of Lakin & Hussaini (1984), Dhanak (1993) and Balachandar & Malik (1995) that the flow becomes more unstable (i.e. exhibits higher growth rates and lower critical Reynolds numbers) as the apex is approached. The present work opens up still further possible reasons for these experimental difficulties. Adverse pressure gradients can trigger flow separations, which even though these may be regular in fashion, nonetheless occur sooner close to the apex (compared with at large distances), and will be susceptible to transition. Further, small changes in pressure gradient can substantially affect the stability characteristics of the flow, as shown in DD. The presence of the leading-edge eigenstates described in § 4 raises yet further possibilities, including that of by-pass transition linked to steady, algebraic (spatial) growth.

Finally, we have been unable as yet to predict which of the two primary states (upper and lower branches) will be observed in practice/experiment; this could depend on the particular details of any given configuration. To attempt to resolve these important issues, the authors are currently undertaking a series of experiments on flows of this type.

The authors gratefully acknowledge the support of NATO and EPSRC, and a number of useful conversations with Professors A. I. Ruban and S. I. Chernyshenko.

Appendix A. Evaluation of $\theta_{0\eta}(\eta = 0)$

Here we determine the value of $\theta_{0\eta}(\eta = 0)$. As noted in § 2 we may set $\alpha = 90^\circ$ without any loss of generality, and then in the limit as $\zeta \to \infty$ we write (in addition to (2.32)–(2.35)) that

$$V^*(\xi, \eta, \zeta) = V_0(\xi, \eta) + O(\zeta^{-2}), \tag{A 1}$$

$$W^*(\xi, \eta, \zeta) = \zeta W_0(\xi, \eta) + O(1), \tag{A 2}$$

$$P(\xi, \eta, \zeta) = \tfrac{1}{2}\zeta^2 \hat{P}_0(\xi, \eta) + O(\zeta). \tag{A 3}$$

From (2.4) we must have that

$$\hat{P}_{0\eta} = 0, \tag{A 4}$$

implying no variation of the secondary pressure across the boundary layer, which, using the crossflow momentum equation (2.5) leads to

$$-\sqrt{2}\hat{P}_0 + W_{0\eta\eta} = U_0(1-n)\left[-2W_0 + \xi W_{0\xi} - \eta W_{0\eta}\right] + \sqrt{2}V_0 W_{0\eta} + \sqrt{2}W_0^2. \tag{A 5}$$

We also note that on account of the flow symmetry about $\eta = \zeta$, as $\eta \to \infty$

$$W_0 \to -\frac{1}{\sqrt{2}}\left[nf(\xi) + \frac{(1-n)}{2}\xi f_\xi\right]. \tag{A 6}$$

Consequently we see that taking the limit as $\eta \to \infty$ of (A 5) together with (A 6) yields

$$P_0 = \frac{\xi f}{4}\left[(1-n^2)f_\xi + \xi(1-n)^2 f_{\xi\xi}\right] - \frac{1}{2}\left[nf + \frac{\xi}{2}(1-n)f_\xi\right]\left[(2-n)f + \frac{\xi}{2}(1-n)f_\xi\right]. \tag{A 7}$$

Taking $\eta = 0$ in (A 5) above leads to

$$W_{0\eta\eta}(\eta = 0) = \sqrt{2}\hat{P}_0 - g(\xi)W_{0\eta}(\eta = 0), \tag{A 8}$$

and from the streamwise momentum equation (2.37) evaluated on $\eta = 0$ we have

$$U_{0\eta\eta}(\eta = 0) = -2nf^2 - \xi(1-n)ff_\xi - g(\xi)U_{0\eta}(\eta = 0). \tag{A 9}$$

Taking (A 5)–(A 8) together leads to the conclusion that

$$\theta_{0\eta}(\eta = 0) = \left[nf(\xi) + \tfrac{1}{2}(1-n)\xi f_\xi\right]^2 - \tfrac{1}{2}\xi f\left[(1-n^2)f_\xi + \xi(1-n)^2 f_{\xi\xi}\right] - g(\xi)\theta_0(\eta = 0). \tag{A 10}$$

This result is important, because it serves to characterize the various families of solution. In particular setting $\xi = 0$, and correspondingly $f(0) = 1$ (i.e. focusing on similarity, rather than developing solutions), leads to

$$\theta_{0\eta}(\eta = 0) = n^2 - g(0)\theta_0(\eta = 0). \tag{A 11}$$

Crucially, this formula characterizes all the far-field family of solutions (with symmetry about $\eta = \zeta$) described in DD. Analogous formulae may be derived in the case of flows without symmetry on $\eta = \zeta$.

Appendix B. The limit of large suction with $n = 0$

Here we consider the large-suction limit as $g(0) \to \infty$ for the zero-pressure gradient case $n = 0$. For convenience we write $\Delta = g(0)$ as a measure of the suction magnitude. Figure 2 clearly shows that the two solution branches remain distinct as suction increases, and must therefore be considered separately. We note that $U_{0\eta}(\eta = 0)$ and $\theta_0(\eta = 0)$ both seem to increase without bound as $\Delta \to \infty$ in both cases. Consider first the two-dimensional branch (which turns out to correspond to the classical results of Pretsch 1944; Watson 1947; and Rosenhead 1966), by writing

$$\Phi_0 = \Delta + \Delta^{-1}\hat{\Phi}_0(\hat{\eta}) + \cdots, \tag{B 1}$$

$$U_0 = \hat{U}_0(\hat{\eta}) + \cdots, \tag{B 2}$$

$$\Psi_0 = \hat{\Psi}_0(\hat{\eta}) + \cdots, \tag{B 3}$$

$$\theta_0 = \Delta\hat{\theta}_0(\hat{\eta}) + \cdots, \tag{B 4}$$

where we define a thin sublayer

$$\eta = \hat{\eta}/\Delta, \quad \hat{\eta} = O(1), \tag{B 5}$$

and we find

$$\hat{U}_0 = 1 - \mathrm{e}^{-\hat{\eta}}, \tag{B 6}$$

$$\hat{\Phi}_{0\hat{\eta}} = \hat{\Psi}_0 = \hat{U}_0, \tag{B 7}$$

$$\hat{\theta}_0 = \hat{U}_{0\hat{\eta}} \tag{B 8}$$

(the first term in the Φ_0 expansion is clearly necessary on direct account of the suction, *per se*). This solution satisfies all the necessary freestream conditions, corresponding to the asymptotic suction profile, and hence completes the description of this solution branch (which we note is confined to a thin, $\eta = O(\Delta^{-1})$ sublayer).

The other (three-dimensional) branch is somewhat more complicated, involving

a multi-layered structure. Our numerical results indicate for this branch that the streamwise shear $U_{0\eta}(\eta = 0)$ increases at approximately the same rate as that of the two-dimensional branch, whilst the value of $\theta_0(0)$ increases quite considerably faster than its two-dimensional counterpart. This (partly) leads us to suggest an asymptotic series of the form

$$U_0 = \hat{U}_0(\hat{\eta}) + \cdots, \tag{B 9}$$

$$\Phi_0 = \Delta + \delta\Delta\hat{\Phi}_0(\hat{\eta}) + \cdots, \tag{B 10}$$

$$\Psi_0 = \delta\Delta^2\hat{\Psi}_0(\hat{\eta}) + \cdots, \tag{B 11}$$

$$\theta_0 = \delta\Delta^3\hat{\theta}_0(\hat{\eta}) + \cdots, \tag{B 12}$$

where $\hat{\eta}$ is defined by (B 5), and we assume implicitly that $1 \gg |\delta| \gg \Delta^{-1}$; at this stage δ is not defined. It is not unreasonable that $\hat{U}_0(\hat{\eta})$ is given by the asymptotic suction profile (B 6), whilst the other leading-order terms are expected to be governed by

$$\hat{\theta}_{0\hat{\eta}\hat{\eta}} + \hat{\theta}_{0\hat{\eta}} = 0, \tag{B 13}$$

$$\hat{\theta}_0 = \hat{\Psi}_{0\hat{\eta}}, \tag{B 14}$$

$$\hat{\Psi}_0 = -\hat{\Phi}_{0\hat{\eta}}, \tag{B 15}$$

and so (implementing the boundary conditions)

$$\hat{\Phi}_0 = A\left[1 - \mathrm{e}^{-\hat{\eta}} - \hat{\eta}\right], \tag{B 16}$$

where $A = \hat{\theta}_0(\hat{\eta} = 0)$ is a constant, and $\hat{\theta}_0$ and $\hat{\Psi}_0$ can be simply inferred from differentiation, via (B 14) and (B 15); indeed, in all that follows the corresponding values of the θ_0 and Ψ_0 quantities may be deduced from these two equations.

Clearly a breakdown must occur when the second-order term of Φ_0 becomes comparable to $O(\Delta)$, i.e. when η increases to

$$\eta = \frac{\tilde{\eta}}{\delta\Delta}, \quad \tilde{\eta} = O(1). \tag{B 17}$$

In this zone, which is much thicker than the previous layer, but still thin compared with the original boundary-layer thickness, the previous solution leads us to expect

$$\Phi_0 = \Delta\tilde{\Phi}_0(\tilde{\eta}) + \delta\Delta\tilde{\Phi}_1(\tilde{\eta}) + \cdots \tag{B 18}$$

(with U_0 unity to leading order) which leads to the following (inviscid) equation:

$$\tilde{\Phi}_{0\tilde{\eta}\tilde{\eta}\tilde{\eta}}\tilde{\Phi}_0 - \tilde{\Phi}_{0\tilde{\eta}}\tilde{\Phi}_{0\tilde{\eta}\tilde{\eta}} = 0. \tag{B 19}$$

An exact solution to the above system seems to be appropriate here, specifically

$$\tilde{\Phi}_0 = \mathrm{e}^{-A\tilde{\eta}} \tag{B 20}$$

(where the constants of integration have been chosen to be consistent with the matching conditions as $\tilde{\eta} \to 0$).

It turns out (for later purposes), that we do need to consider higher-order quantities: in particular we demand that viscous effects are important in this respect, and the requirement to match with the exponentially small term in (B 16), and this leads to the 'solution'

$$\tilde{\Phi}_{1\tilde{\eta}\tilde{\eta}\tilde{\eta}} = A\exp\left[(\mathrm{e}^{-A\tilde{\eta}} - 1)/A\delta\right]. \tag{B 21}$$

The associated quantities may be deduced from (B 14) and (B 15), with the subscript zeros replaced by ones. Although these quantities are very small, nonetheless it will be seen they play an important role at a later stage. Yet another breakdown occurs, when $\tilde{\eta}$ increases, specifically when

$$\tilde{\eta} = O(-(1/A)\log\delta), \tag{B 22}$$

where the viscous term becomes important again to leading order. To describe this region we write the solution in the following form:

$$\eta = -\frac{1}{A\Delta\delta}\log\delta + \frac{1}{\Delta\delta}\eta^*, \quad \eta^* = O(1), \tag{B 23}$$

$$\Phi_0 = \Delta\delta\Phi_0^*(\eta^*) + \cdots + E\Delta\delta^2\Phi_1^* + \cdots, \tag{B 24}$$

where

$$E = \mathrm{e}^{-1/A\delta}. \tag{B 25}$$

Note that although, notionally, the E-terms are exponentially small, nonetheless this turns out to be crucial below. The $\eta^* = O(1)$ zone corresponds to a relatively thick displaced layer, and leads to the system

$$\Phi^*_{0\eta^*\eta^*\eta^*\eta^*} + \Phi_0^*\Phi^*_{0\eta^*\eta^*\eta^*} - \Phi^*_{0\eta^*\eta^*}\Phi^*_{0\eta^*} = 0. \tag{B 26}$$

Again, somewhat fortuitously, an exact, relevant solution of this system may be obtained, given by

$$\Phi_0^* = A + \mathrm{e}^{-A\eta^*}. \tag{B 27}$$

The $O(E)$ (seemingly exponentially small) terms are determined from a linearized form of (B 26), i.e.

$$\Phi^*_{1\eta^*\eta^*\eta^*\eta^*} + \Phi_1^*\Phi^*_{0\eta^*\eta^*\eta^*} + \Phi_0^*\Phi^*_{1\eta^*\eta^*\eta^*} - \Phi^*_{1\eta^*\eta^*}\Phi^*_{0\eta^*} - \Phi^*_{0\eta^*\eta^*}\Phi^*_{1\eta^*} = 0, \tag{B 28}$$

and it seems not unreasonable to demand that $|\Phi_1^*| \gg \mathrm{e}^{-A\eta^*}$ as $\eta^* \to \infty$, a property that will be used below. The next breakdown occurs when Ψ_0 becomes $O(1)$, which turns out to have the same thickness as the previous $\eta^* = O(1)$ layer, but further displaced from the wall. This is accomplished by setting

$$\eta = -\frac{1}{A\Delta\delta}\log\delta + \frac{1}{\Delta\delta A}\log(\delta^2\Delta^2) + \frac{\eta_1}{\delta\Delta}, \quad \eta_1 = O(1), \tag{B 29}$$

with

$$\Phi_0 = \Delta\delta A + \frac{1}{\Delta\delta}\bar{\Phi}_0(\eta_1) + \cdots, \tag{B 30}$$

and $U_0 = 1$ in this zone to leading order, again.

This leads to the solution

$$\bar{\Phi}_0 = \eta_1 + \mathrm{e}^{-A\eta_1} + C_1, \tag{B 31}$$

where C_1 is some constant (undetermined to this order).

In order to match with the $\eta^* \to \infty$ solution (in particular with the higher-order terms), we must have to leading order

$$A\delta \approx \frac{1}{2\log\Delta}. \tag{B 32}$$

The fact that A and δ are determined together is not surprising, given that these

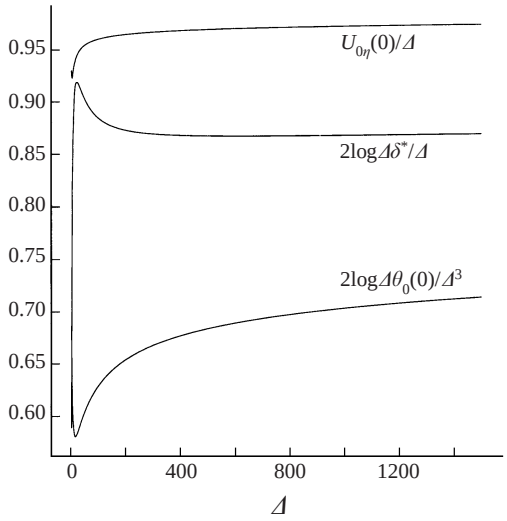

FIGURE 12. Variation of $U_{0\eta}(\eta = 0)$, δ^* and $\theta(\eta = 0)$ with Δ (suction parameter), $n = 0$.

quantities appear together to leading order. Note that higher-order terms are likely to affect (B 32), leading to $\log\log\Delta$ and higher terms. Figure 12 shows the variation of numerically calculated values of $2\log\Delta\theta_0(\eta = 0)/\Delta^3$, $2\log\Delta\delta^*/\Delta$ and $U_{0\eta}(\eta = 0)/\Delta$ with $\Delta = g(0)$, where $\delta^* = [\Phi_0(\eta) - \eta]_{\eta\to\infty}$, quantities that should approach unity as $\Delta \to \infty$. The agreement with the asymptotic theory is not unsatisfactory, particularly given the 'largeness' of the small parameter $1/\log\Delta$ even at the higher values of Δ, and the likely (significant) correction terms of the form $\log\log\Delta$ which, as pointed out above, are likely to occur a higher order. The solution therefore takes on a four-tiered structure, this feature distinguishing this solution branch from the other (two-dimensional) solution branch described earlier.

Appendix C. The limits of blowing ($n = 0$)

Consider next other aspects of the results shown in figure 2, showing the variation of the shear stress distribution, for $n = 0$, with $g(0)$, in particular in the limit as the flow separates, i.e. as $U_{0\eta}(\eta = 0) \to 0$. We note that solutions cease to exist beyond this limit (indeed, it is hardly surprising the zero pressure gradient condition does not exhibit reversed-flow solutions), and figure 2 shows that four such critical points exist. The point $g(0) = -C_{2D} = -0.875747\ldots$ corresponds to the classical two-dimensional result, as detailed in Rosenhead (1966). The three other terminal points all represent truly three-dimensional flows. These occur at $g(0) = -C_{3Da} = -1.18727\ldots$, $g(0) = -C_{3Db} = -0.66204\ldots$, and finally as $g(0) \to 0$. With the exception of this last case (which will be considered independently, later), for all cases the limit as $g(0) \to -C_{(n)}$ can be considered simultaneously; note that for C_{2D} we have the two-dimensional conditions detailed in (B 7), (B 8), namely

$$U_0 = \Psi_0 = \Phi_0'(\bar{\eta}), \tag{C 1}$$

$$\theta_0 = \Phi_0''(\bar{\eta}). \tag{C 2}$$

Inspection of the solutions close to these critical (terminal) values clearly reveals a displaced shear layer behaviour, the location of which increases without bound as the

critical value of $g(0)$ is approached. Indeed this shear layer behaviour is found to be quite a universal flow feature. In order to understand the flow as $g(0) \to -C_{(n)}$, we write

$$g(0) = -C_{(n)} + \epsilon_1, \tag{C 3}$$

where $0 < \epsilon_1 \ll 1$. Turning first to the shear layer itself, assuming this becomes increasingly displaced from the wall, it is appropriate to set

$$\eta = \Lambda + \bar{\eta}, \tag{C 4}$$

where $\Lambda(\epsilon_1) \gg 1$, and $\bar{\eta} = O(1)$, together with

$$\begin{aligned} U_0 &= U_{00}(\bar{\eta}) + \cdots, \quad \Phi_0 = \Phi_{00}(\bar{\eta}) + \cdots, \\ \Psi_0 &= \Psi_{00}(\bar{\eta}) + \cdots, \quad \theta_0 = \theta_{00}(\bar{\eta}) + \cdots. \end{aligned} \tag{C 5}$$

This assumes the shear layer remains of thickness comparable to the original boundary-layer thickness. The governing equations are then

$$2U_{00} = \Phi_{00\bar{\eta}} + \Psi_{00}, \tag{C 6}$$

$$U_{00\bar{\eta}\bar{\eta}} + \Phi_{00} U_{00\bar{\eta}} = 0, \tag{C 7}$$

$$\theta_{00} = \Psi_{00\bar{\eta}}, \tag{C 8}$$

$$\theta_{00\bar{\eta}\bar{\eta}} - 2U_{00}U_{00\bar{\eta}} + \theta_{00\bar{\eta}}\Phi_{00} + \Psi_{00}\theta_{00} + 2U_{00}\theta_{00} = 0. \tag{C 9}$$

The boundary conditions to be applied to this system as $\bar{\eta} \to \infty$ are that free-stream conditions are approached, i.e. that

$$U_{00}(\bar{\eta}) \to 1, \quad \Phi_{00\bar{\eta}} \to \Psi_{00} \to 1, \quad \theta_{00} \to 0. \tag{C 10}$$

This may be regarded as a three-dimensional (incompressible) counterpart of the Chapman (1950) shear layer problem, and as such the appropriate boundary conditions as $\bar{\eta} \to -\infty$ are

$$U_{00}(\bar{\eta}), \Phi_{00\bar{\eta}}(\bar{\eta}), \Psi_{00}(\bar{\eta}), \theta_{00}(\bar{\eta}) \to 0, \tag{C 11}$$

corresponding to relatively stagnant conditions below the shear layer. Results for the $U_{00}(\bar{\eta})$ and $W_{00}(\bar{\eta})$ profiles are shown in figure 13 where the solid line relates to the C_{3Da} root, the short-dashed line to the C_{3Db} root and the long-dashed line to the C_{2D} root (which we note has $W_{00} \equiv 0$). The conditions as $\bar{\eta} \to -\infty$ above may be refined (and this will be necessary for later purposes) to the following

$$\Phi_{00}(\bar{\eta}) \to -C_{(n)} + \alpha_1 \mathrm{e}^{C_{(n)}\bar{\eta}} + \cdots, \tag{C 12}$$

$$U_{00}(\bar{\eta}) \to \alpha_2 \mathrm{e}^{C_{(n)}\bar{\eta}} + \cdots, \tag{C 13}$$

$$\Psi_{00}(\bar{\eta}) \to \alpha_3 \mathrm{e}^{C_{(n)}\bar{\eta}} + \cdots, \tag{C 14}$$

$$\theta_{00}(\bar{\eta}) \to \alpha_4 \mathrm{e}^{C_{(n)}\bar{\eta}} + \cdots, \tag{C 15}$$

where $\alpha_3 = 2\alpha_2 - \alpha_1 C_{(n)}$ and $\alpha_4 = C_{(n)}\alpha_3$. As with the Chapman (1950) problem, there is no absolute origin to the $\bar{\eta}$-coordinate; we are at liberty to arbitrarily specify this (in principle the determination of this can be achieved at higher order and incorporated into Λ) and to this end we set $\Phi_{00}(\bar{\eta} = 0) = 0$. Our computations then led to the following values (where here we define $\delta^* = [\Phi(\bar{\eta}) - \bar{\eta}]_{\bar{\eta}\to\infty}$): for C_{2D}, $\alpha_1 = 1.1549\ldots$, $\alpha_2 = 1.01143\ldots$ (with $\alpha_3 = \alpha_2$), $\delta^* = -0.37396\ldots$; for C_{3Da} $\alpha_1 = 1.0109\ldots$, $\alpha_2 = 1.709\ldots$, $\delta^* = 0.313\ldots$ (intriguingly our computations for this case, undertaken with some care, suggested that $|\alpha_3| < 10^{-5}$, very strongly pointing

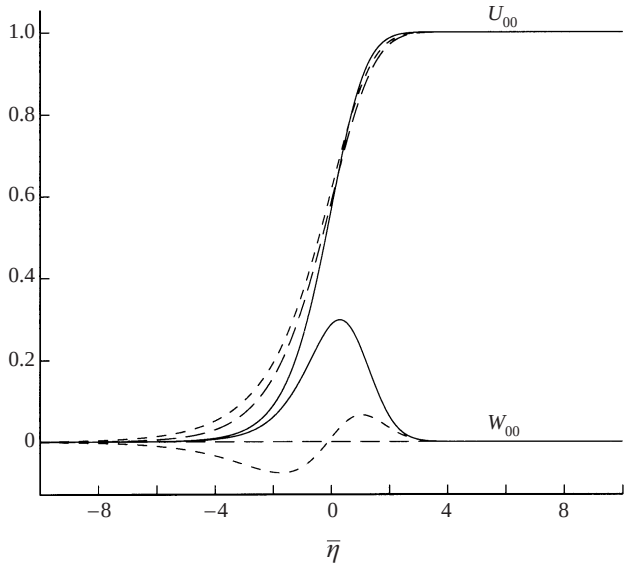

FIGURE 13. U_{00} and W_{00} profiles across the asymptotic shear layer.

to the condition that $\alpha_3 = \alpha_4 = 0$, implying $2\alpha_2 = \alpha_1 C_{3Da}$); for C_{3Db}, $\alpha_1 = -0.1506\ldots$, $\alpha_2 = 0.7233\ldots$, $\delta^* = -0.16547\ldots$.

As noted above, to leading order the region between the wall and the shear layer is one of relatively stagnant flow ($|U_0| \ll 1$), with uniform $\Phi_0 = -C_{(n)}$. We next consider the second-order terms in this region (retaining the original η variable), writing

$$\Phi_0 = -C_{(n)} + \epsilon_1 \tilde{\Phi}_{01}(\eta) + \cdots, \tag{C 16}$$

with

$$\eta = O(1), \tag{C 17}$$

and we must therefore have that

$$U_0 = \epsilon_1 \tilde{U}_{01}(\eta) + \cdots \tag{C 18}$$

(Φ_0, Ψ_0 and θ_0 are also $O(\epsilon_1)$ in this region). The only meaningful result (imposing no slip on $\eta = 0$) is that

$$\tilde{U}_{01}(\eta_1) = C_1(1 - \mathrm{e}^{C_{(n)}\eta}), \tag{C 19}$$

where C_1 is a constant, whilst proper matching between this zone (C 19) and the shear layer (C 13) requires

$$\Lambda \approx -\frac{\log \epsilon_1}{C_{(n)}}, \tag{C 20}$$

and C_1 must be determined at higher order.

Turning now to the terminal point at $g(0) = 0$, in this case again inspection of the velocity (and other) profiles strongly suggests that a massively displaced shear layer of the form (C 6)–(C 11) is appropriate. We set in this case $g(0) = -\epsilon_1$, and consider the limit $\epsilon_1 \to 0$. Further, figure 14 shows $\Phi_0(\eta)$ (broken line) and $U_0(\eta)$ (solid line) profiles at $g(0) = -0.2, -0.15, -0.1$. It is quite clear that the shear layer is of the form described above, for the particular case corresponding to C_{3Da}, but instead of

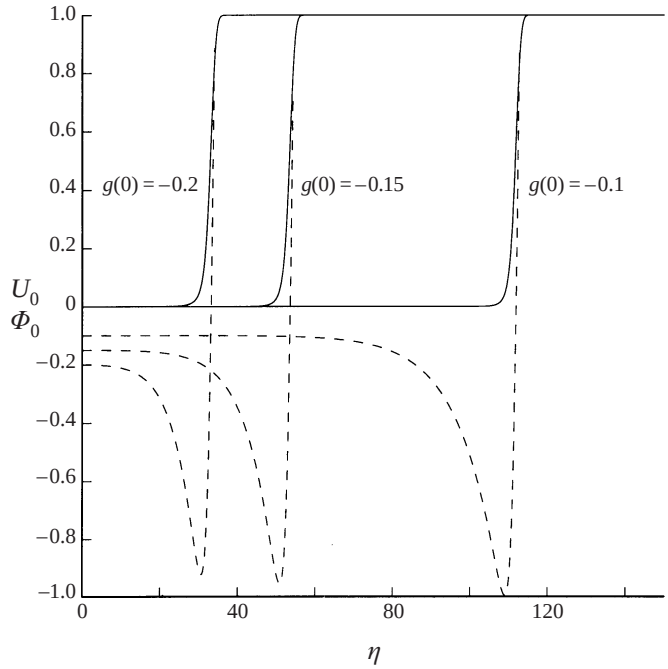

FIGURE 14. U_0 and Φ_0 profiles for $g(0)$ as indicated, $n = 0$.

a region of relatively uniform Φ_0 between this shear layer and the wall (as occurs in the previous three terminal states), in the present case this can no longer be so.

Close inspection of our numerical results suggests that in the region between the wall and some distance off the wall, $\Phi_0 \approx g(0)$. Further, since it is possible to show (see Appendix A) that for $n = 0$, $\theta_{0\eta}(0) = -g(0)\theta_0(0)$, then the appropriate lengthscale is $\eta = O(1/\epsilon_1)$. However in this region the indication from our computations is also that $|\Psi_0|$, $|\theta_0|$ are exceedingly small (certainly at least exponentially small), and $|U_0|$ is even smaller. Taken together, these trends suggest we need to define the thick scale

$$\eta = \frac{\eta_2}{\epsilon_1}, \quad \eta_2 = O(1), \tag{C 21}$$

wherein

$$\Phi_0 = -\epsilon_1 + \delta\Phi_{01}(\eta_2) + \cdots, \tag{C 22}$$

$$\Psi_0 = \delta\epsilon_1\Psi_{01}(\eta_2) + \cdots, \tag{C 23}$$

$$\theta_0 = \delta\epsilon_1^2\theta_{01}(\eta_2) + \cdots, \tag{C 24}$$

and $|U_0|$ is again even smaller than any of the other three basic quantities, and here $|\delta| \ll \epsilon_1$ and will be determined later.

The solution of the above quantities is then straightforward, yielding

$$\Phi_{01} = A_0\,[\mathrm{e}^{\eta_2} - \eta_2 - 1]\,, \tag{C 25}$$

$$\Psi_{01} = -A_0\,[\mathrm{e}^{\eta_2} - 1]\,, \tag{C 26}$$

$$\theta_{01} = -A_0\mathrm{e}^{\eta_2}, \tag{C 27}$$

where A_0 is a constant. There must then be a breakdown of the above when the $O(\delta)$

and $O(\epsilon_1)$ terms in the Φ_0 expansions become comparable. This occurs when

$$\eta = \epsilon_1^{-1} \log(\epsilon_1/\delta) + \epsilon_1^{-1}\tilde{\eta}, \tag{C 28}$$

wherein $\tilde{\eta} = O(1)$, and

$$\Phi_0 = \epsilon_1 \tilde{\Phi}(\tilde{\eta}) + \cdots + \delta \log(\epsilon_1/\delta)\tilde{\Phi}_1(\tilde{\eta}) + \cdots \ . \tag{C 29}$$

The dots after the leading term denote intermediate-order terms, which are not important for our purposes. Again we have that $|U_0| \ll |\Phi_0|$. This leads to the following equation for $\tilde{\Phi}$:

$$\tilde{\Phi}_{\tilde{\eta}\tilde{\eta}\tilde{\eta}} + \tilde{\Phi}\tilde{\Phi}_{\tilde{\eta}\tilde{\eta}} - \tilde{\Phi}_{\tilde{\eta}}^2 = 0, \tag{C 30}$$

with, as $\tilde{\eta} \to -\infty$,

$$\tilde{\Phi} \to -1 + A_0 \mathrm{e}^{\tilde{\eta}}, \tag{C 31}$$

where A_0 is a positive constant. Indeed, it seems that (C 31) is a perfectly acceptable exact solution of (C 30) for all values of $\tilde{\eta}$.

The higher-order (subscript 1) quantities are determined through a linearized form of (C 30), namely

$$\tilde{\Phi}_{1\tilde{\eta}\tilde{\eta}\tilde{\eta}} + \tilde{\Phi}\tilde{\Phi}_{1\tilde{\eta}\tilde{\eta}} + \tilde{\Phi}_1\tilde{\Phi}_{\tilde{\eta}\tilde{\eta}} - 2\tilde{\Phi}_{\tilde{\eta}}\tilde{\Phi}_{1\tilde{\eta}} = 0, \tag{C 32}$$

from which it seems that as $\tilde{\eta} \to \infty$

$$\tilde{\Phi}_{1\tilde{\eta}\tilde{\eta}\tilde{\eta}} \sim -A_1 \exp(A_0 \mathrm{e}^{\tilde{\eta}}), \tag{C 33}$$

where A_1 is a constant.

A further breakdown will occur when the leading-order flow quantities become $O(1)$, i.e. when

$$\tilde{\eta} = -\log \epsilon_1. \tag{C 34}$$

This then leads to a regime where Φ_0, U_0, Ψ_0 and θ_0 are all $O(1)$, determined by the system (C 6)–(C 11), with $\{U_{00}, \Phi_{00}, \Psi_{00}, \theta_{00}\}$ replaced by $\{U_0, \Phi_0, \Psi_0, \theta_0\}$, with

$$\eta = \epsilon_1^{-1} \log \frac{1}{\delta} + \bar{\eta}, \quad \bar{\eta} = O(1). \tag{C 35}$$

This corresponds to a grossly displaced shear layer, whose thickness is comparable to that of the original boundary-layer thickness encountered earlier. In order that there is a proper match between the $\tilde{\eta} = O(1)$ and $\bar{\eta}$ regimes we require

$$A_0 = C_{3Da} \tag{C 36}$$

which confirms the positive value of A_0. If we now (reasonably) assume that the subscript 1 term in (C 29) also becomes $O(1)$ (or at least $\gg O(\delta)$) in the shear layer, then we are led to the conclusion that

$$\delta \approx \mathrm{e}^{-A_0/\epsilon_1}. \tag{C 37}$$

This leads to the further conclusion that the location of the shear layer is given by $\eta \approx O(\epsilon_1^{-2})$. Indeed, figure 15 shows the variation of $-\epsilon_1 \log(\theta_0(\eta = 0))$ and $-\log \delta^* / \log \epsilon_1$ with ϵ_1 (where $\delta^* = [\Phi_0(\eta) - \eta]_{\eta \to \infty}$), which according to our asymptotic approach given above should approach C_{3Da} and 2 respectively; the agreement with our numerical results is encouraging, particularly given the preponderance of logarithmic terms in the analysis. (Unfortunately computations beyond $g(0) = -\epsilon_1 \approx -0.075$ proved prohibitive, and results are therefore terminated at this value.)

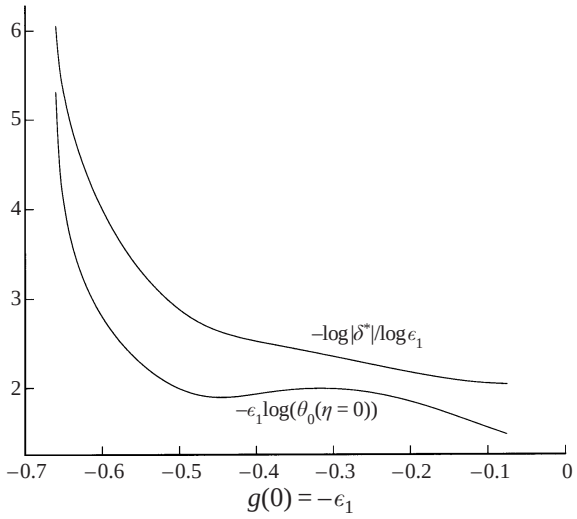

FIGURE 15. Variation of $\theta_0(\eta = 0)$ and δ^* with $\epsilon_1 = -g(0)$.

Appendix D. The limit as $n \to 0-$ (displaced shear-layer, reversed-flow solution branches, no transpiration)

Here we address the question of the nature of the small solution branch as $n \to 0-$, i.e. the branch close to the origin in figure 1(*a*) (for the choice $g(0) = 0$), a question that turns out to be inherently coupled to the work in the previous Appendices.

It is well known (Rosenhead 1966) that the two-dimensional Falkner–Skan family of solutions exhibits a degree of non-uniqueness for $n < 0$, with a second class of solutions which exhibit backflow (the extent of the reversed-flow region increasing without bound as $n \to 0-$ in our notation). In the present work, an analogous class of solution arises, although in our case these solutions are not directly connected to the primary solution branch (as n varies), but appear as an independent branch. This branch, itself, involves two solutions (making a total of four solutions for $n \to 0-$).

Treating $|n|$ as our small parameter, we suggest the η domain decomposes into two distinct zones. As $n \to 0-$, observed shear layers form in both the upper and lower branches and (C 4) is again appropriate, but here we take $\Lambda \equiv \Lambda(n) \to \infty$ as $n \to 0-$. The nature of the flow profiles ($U_0(\eta)$ and $\Phi_0(\eta)$) is shown in figures 16(*a*) and 16(*b*), for $n = -0.009, -0.006, -0.004$. The solid lines correspond to the lower portion of this particular solution branch (i.e. $\theta_0(\eta) < 0$), the broken lines to the upper portion. Figure 16(*b*) suggests that the shear layer is described by (C 6)–(C 11), again for the particular case considered above $\Phi_{00}|_{\bar{\eta}\to-\infty} = C_{3Da}$, for both solution branches.

Therefore, fortunately no further computations are necessary for this aspect of the work, since we are able to determine all the information required from our transpiration results, in particular those shown in figure 13. The details of the shear layer correspond precisely with the limiting values of $g(0) \to C_{3Da}$ for which both $\theta_0(\eta)$ and $U_{0\eta}(0)$ approach zero.

We now consider the layer that forms between the wall and the shear layer. This turns out to be quite thick in comparison with the original boundary layer, as well as the shear layer. The solution develops in the following manner

$$U_0 = |n|^{1/2}\tilde{U}_{00}(\tilde{\eta}) + \cdots, \tag{D 1}$$

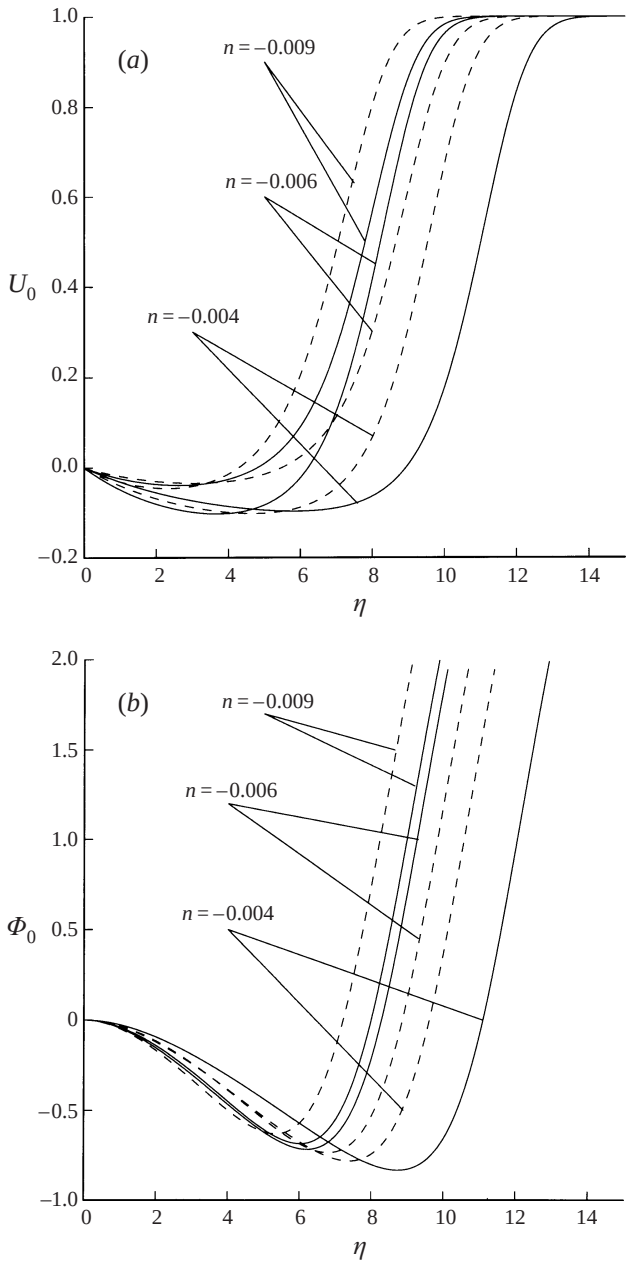

FIGURE 16. (*a*) U_0 profiles and (*b*) Φ_0 profiles, $g(0) = 0$, n as indicated.

$$\Phi_0 = |n|^{1/4}\tilde{\Phi}_{00}(\tilde{\eta}) + \cdots, \tag{D 2}$$

$$\Psi_0 = |n|^{1/2}\tilde{\Psi}_{00}(\tilde{\eta}) + \cdots, \tag{D 3}$$

$$\theta_0 = |n|^{3/4}\tilde{\theta}_{00}(\tilde{\eta}) + \cdots, \tag{D 4}$$

with

$$\eta = |n|^{-1/4}\tilde{\eta}. \tag{D 5}$$

These lead to the following system of equations (assuming $n < 0$):

$$2\tilde{U}_{00} = \tilde{\Phi}_{00\tilde{\eta}} + \tilde{\Psi}_{00}, \tag{D 6}$$

$$\tilde{\theta}_{00} = \tilde{\Psi}_{00\tilde{\eta}}, \tag{D 7}$$

$$\tilde{U}_{00\tilde{\eta}\tilde{\eta}} - 2 + \tilde{\Phi}_{00}\tilde{U}_{00\tilde{\eta}} = 0, \tag{D 8}$$

$$\tilde{\theta}_{00\tilde{\eta}\tilde{\eta}} - 2\tilde{U}_{00}\tilde{U}_{00\tilde{\eta}} + \tilde{\theta}_{00\tilde{\eta}}\tilde{\Phi}_{00} + \tilde{\Psi}_{00}\tilde{\theta}_{00} + 2\tilde{U}_{00}\tilde{\theta}_{00} = 0, \tag{D 9}$$

with

$$\tilde{U}_{00}(\tilde{\eta} = 0) = \tilde{\Phi}_{00}(\tilde{\eta} = 0) = \tilde{\Psi}_{00}(\tilde{\eta} = 0) = \tilde{\theta}_{00\tilde{\eta}}(\tilde{\eta} = 0) = 0. \tag{D 10}$$

Inspection of the above system as $\tilde{\eta} \to \infty$ suggests the following behaviour:

$$\tilde{\Phi}_{00} \sim A_{00}\tilde{\eta}\sqrt{\log\tilde{\eta}} + \cdots, \tag{D 11}$$

$$\tilde{U}_{00} \sim \frac{4}{A_{00}}\sqrt{\log\tilde{\eta}} + \cdots, \tag{D 12}$$

$$\tilde{\Psi}_{00} \sim \left(\frac{8}{A_{00}} - A_{00}\right)\sqrt{\log\tilde{\eta}} + \cdots, \tag{D 13}$$

$$\tilde{\theta}_{00} \sim \frac{1}{2\tilde{\eta}\sqrt{\log\tilde{\eta}}}\left(\frac{8}{A_{00}} - A_{00}\right) + \cdots, \tag{D 14}$$

where four values of A_{00} are possible, namely

$$A_{00} = \pm 2, \pm\sqrt{12}. \tag{D 15}$$

The next stage in the solution process is best seen by inspection of the $\tilde{\Phi}_{00}$ term. In particular we see that $\Phi_0 = O(1)$ when $\eta \approx O([|n|\log|n|^{-1/4}]^{-1/2})$. Using this result enables us to match with the shear layer and leads first to

$$\Lambda \approx \eta_0[|n|\log|n|^{-1/4}]^{-1/2}, \quad \eta_0 = O(1), \tag{D 16}$$

and secondly to

$$A_{00}\eta_0 = -C_{3Da}. \tag{D 17}$$

Because $C_{3Da} > 0$ the only meaningful conclusion is that $A_{00} = -2, -\sqrt{12}$. These both correspond to reversed flow in this sublayer, and also highlight the non-uniqueness found numerically in the problem. The region between the shear layer and the $O(|n|^{-1/4})$ zone is basically an inviscid one, and is somewhat passive in nature, comprising just a uniform, slow (reversed) flow. We therefore have the two values of η_0 being given by $\eta_0 \approx C_{3Da}/2, C_{3Da}/\sqrt{12}$. These results are not inconsistent with the results shown in figures 16(a) and 16(b). There was clear evidence in our numerical results of the minimum of Φ_0 reducing as $n \to 0-$; there was absolutely no evidence of this approaching any value other than $-C_{3Da}$, and other numerical results (not shown here), strongly point to the the minimum value of U_0 decreasing in magnitude as $n \to 0-$, consistent with the asymptotic results above. We note that the above results are in quite close agreement with those of Stewartson (1954), who used a somewhat more heuristic treatment of the problem for the two-dimensional limiting case (although this is not directly relevant here). Finally note that the choice $A_{00} = -2$ is likely to give rise to $\theta_0(0) < 0$ (lower branch solution), whilst $A_{00} = -\sqrt{12}$ is likely to lead to $\theta_0(0) > 0$ and hence the upper branch solution. In this respect, it is worth

mentioning the work of Smith (1984), in which two-dimensional, grossly separated Chapman layers were also encountered.

REFERENCES

Abdulwanis, O. A. 1997 Problems in three-dimensional boundary layers. PhD dissertation, University of Manchester.

Balachandar, S. & Malik, M. R. 1995 Inviscid instability of streamwise corner flow. *J. Fluid Mech.* **282**, 187 (also *ICASE Rep.* 93-54).

Bertolotti, F. P. 1997 Response of the Blasius boundary layer to free-stream velocity. *Phys. Fluids* **9**, 2286.

Bertolotti, F. P. & Kendall, J. M. 1997 Response of the Blasius boundary layer to controlled free-stream vortices of axial form. *AIAA Paper* 97-2018.

Brown, S. N. & Stewartson, K. 1975 A non-uniqueness of the hypersonic boundary layer. *Q. J. Mech. Appl. Maths* **28**, 75.

Chapman, D. R. 1950 Laminar mixing of a compressible fluid. *NACA Rep.* 958.

Desai, S. S. & Mangler, K. W. 1974 Incompressible laminar boundary layer flow along a corner formed by two intersecting planes. *RAE TR* 74062.

Dhanak, M. R. 1993 On the instability of flow in a streamwise corner. *Proc. R. Soc. Lond.* A **441**, 203; see also Errata **443**, 624 (1993).

Dhanak, M. R. & Duck, P. W. 1997 The effects of freestream pressure gradient on a corner boundary layer. *Proc. R. Soc. Lond.* A **453**, 1793 (referred to herein as DD).

Ghia, K. N. 1975 Incompressible streamwise flow along an unbounded corner. *AIAA J.* **13**, 902.

Goldstein, S. 1948 On laminar boundary-layer flow near a point of separation. *Q. J. Mech. Appl. Maths* **1**, 43.

Lakin, W. D. & Hussaini, M. Y. 1984 Stability of the laminar boundary layer in a streamwise corner. *Proc. R. Soc. Lond.* A **393**, 101.

Libby, P. A. & Fox, H. 1963 Some perturbation solutions in laminar boundary-layer flows. *J. Fluid Mech.* **17**, 433.

Luchini, P. 1996 Reynolds-number-independent instability of the boundary layer over a flat surface. *J. Fluid Mech.* **327**, 101.

Mikhailov, V. V., Neiland, V. Ya. & Sychev, V. V. 1971 The theory of viscous hypersonic flow. *Ann. Rev. Fluid Mech.* **3**, 371.

Neiland, V. Y. 1970 Upstream propagation of perturbations in a hypersonic flow with a boundary layer. *Akad. Nauk. SSSR Izv. Mekh. Zhid. i Gaza* **4**, 40.

Pal, A. & Rubin, S. G. 1971 Asymptotic features of the viscous flow along a corner. *Q. Appl. Maths* **29**, 91.

Phillips, W. R. 1996 On a class of unsteady boundary layers of finite extent. *J. Fluid Mech.* **319**, 151.

Pretsch, J. 1944 Die laminare Grenzschichte bei starken Absangen und Ausblasen. *Untermath. Mitt. Dtsch. Luftfahrth* 3091.

Ridha, A. 1992 On the dual solutions associated with boundary-layer equations in a corner. *J. Engng Maths* **26**, 525.

Rizzetta, D. P., Burggraf, O. R. & Jenson, R. 1978 Triple-deck solutions for viscous supersonic and hypersonic flow past corners. *J. Fluid Mech.* **89**, 535.

Rosenhead, L. 1966 *Laminar Boundary Layers.* Oxford University Press.

Rubin, S. G. 1966 Incompressible flow along a corner. *J. Fluid Mech.* **26**, 97.

Rubin, S. G. 1982 A review of marching procedures for parabolized Navier–Stokes equations. *Proc. Symp. on Numerical and Physical Aspects of Aerodynamic Flows* (ed. T. Cebeci), p. 171. Springer.

Rubin, S. G. & Grossman, B. 1971 Viscous flow along a corner: numerical solution of the corner layer equations. *Q. Appl. Maths* **29**, 169.

Smith, F. T. 1984 Non-uniqueness in wakes and boundary layers. *Proc. R. Soc. Lond.* A **391**, 1.

Stewartson, K. 1954 Further solutions of the Falkner–Skan equations. *Proc. Camb. Phil. Soc.* **50**, 454.

Stewartson, K. & Williams, P.G. 1969 Self-induced separation. *Proc. R. Soc. Lond.* A **312**, 181.

Watson, E. J. 1947 The asymptotic theory of boundary-layer flow with suction. *Rep. Mem. Aero. Res. Coun. Lond.* 2619.

Wilkinson, S. R. & Zamir, M. 1984 Cross-flow and vorticity patterns in the corner boundary layer at different corner angles. *Aero. Q.* **35**, 309.

Zamir, M. 1973 Further solution of the corner boundary layer equations. *Aero. Q.* **24**, 219.

Zamir, M. 1981 Similarity and stability of the laminar boundary layer in a streamwise corner. *Proc. R. Soc. Lond.* A **377**, 269.